Computational and experimental studies of reactive intermediates in glycosylation reactions

Remmerswaal, W.A.

Chapter 9

Backside versus Frontside S_N2 Reactions of Alkyl Triflates and Alcohols

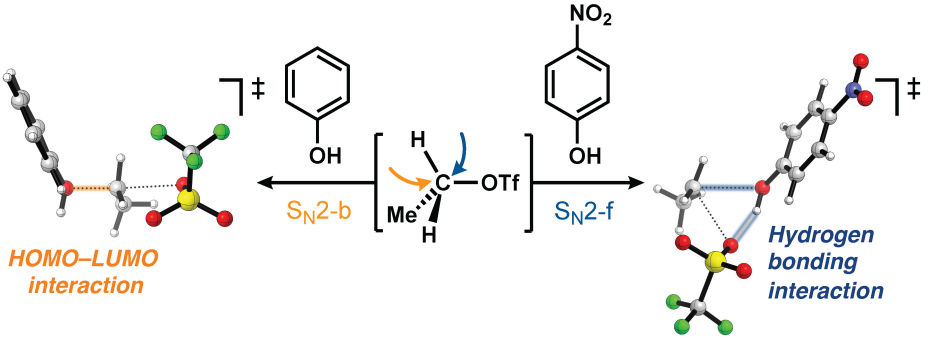

Abstract | Nucleophilic substitution reactions are elementary reactions in organic chemistry that are used in many synthetic routes. By quantum chemical methods, the intrinsic competition between the backside S_N2 (S_N2-b) and frontside S_N2 (S_N2-f) pathways was investigated using a set of simple alkyl triflates as the electrophiles in combination with a systematic series of phenols and partially fluorinated ethanol nucleophiles. It is revealed how and why the well-established mechanistic preference for the S_N2-b pathway slowly erodes and can even be overruled by the unusual S_N2-f substitution mechanism going from strong to weak alcohol nucleophiles. Activation strain analyses disclose that the S_N2-b pathway is favored for strong alcohol nucleophiles because of the well-known intrinsically more efficient approach to the electrophile resulting in a more stabilizing nucleophile–electrophile interaction. In contrast, the preference of weaker alcohol nucleophiles shifts to the S_N2-f pathway, benefiting from a stabilizing hydrogen bond interaction between the incoming alcohol and the leaving group. This hydrogen bond interaction is strengthened by the increased acidity of the weaker alcohol nucleophiles, thereby steering the mechanistic preference toward the frontside S_N2 pathway.

Published | Remmerswaal, W. A.; de Jong, T.; van de Vrande, K. N. A.; Louwersheimer, R.; Verwaal, T.; Filippov, D. V.; Codée, J. D. C.; Hansen, T. *Chem. Eur. J.* **2024**, e202400590.

Introduction

A fundamental challenge in chemical research is the rational design of chemical reactions. Uncovering the operative mechanisms that steer chemical reactivity paves the way for tuning the reactivity of systems toward the desired pathway to avoid unwanted side reactions. The backside bimolecular nucleophilic substitution (S_N2-b) is an elementary reaction in synthetic chemistry.[1–4] Besides being in competition with S_N1-type substitutions, the less common frontside S_N2 (S_N2-f) substitution can also play a role.[5–9] In general, the regular S_N2-b substitution proceeds with the inversion of configuration at the carbon atom under substitution (Walden inversion), and is substantially more efficient than the alternative S_N2-f reaction, which proceeds with retention of configuration (Scheme 1). Both experimental[10–13] and computational[14–24] studies have provided valuable insights into the processes that dictate the S_N2-b versus S_N2-f competition.

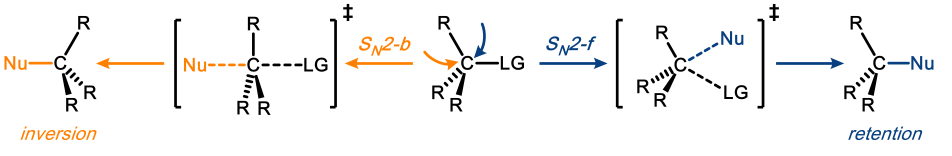

Scheme 1. S_N2-b (orange) and S_N2-f (blue) pathways. Nu = nucleophile, LG = leaving group.

The dominance of the S_N2-b reaction stems from the less sterically demanding approach of the nucleophile at the electrophile (*i.e.*, substrate). The S_N2-f reaction, on the other hand, requires the nucleophile to attack at the same side of the carbon atom, where the leaving group departs, causing closed-shell repulsion. Another factor contributing to the higher reaction barriers found for S_N2-f reactions is the loss of the primary stabilizing $HOMO_{nucleophile}$–$LUMO_{electrophile}$ interaction because most of the orbital amplitude of the electrophiles' LUMO is located at the backside. Both the S_N2-b and S_N2-f are accelerated as the basicity of the incoming nucleophile increases (*i.e.*, better electron-donating capacity) or the carbon–leaving group bond becomes weaker.[17]

However, in specific cases, the S_N2-f pathway has been noted to be a significant or even dominant competing reacting pathway. These substitution reactions show unexpectedly high degrees of retention of stereochemistry.[25–34] For example, the solvolysis of 1-phenylethyl chloride using phenol nucleophiles has been shown to result in phenol ethers with up to 97% retention of configuration at the benzylic carbon.[25] These relatively acidic nucleophiles have been implicated in forming hydrogen bonds during the solvolysis reactions, stabilizing the corresponding frontside transition states over the backside counterparts. *Ab initio* molecular dynamic simulations of chemical glycosylation reactions involving a trichloroacetimidate leaving group have revealed that these reactions may proceed with S_N2-f character.[35] Here, the analogy to retaining glycosyl transferase enzymes becomes apparent.[36–42] These enzymes have been shown to transfer carbohydrate monosaccharides from a nucleotide diphosphate sugar donor to alcohol acceptors (often other carbohydrates) with retention of configuration at the anomeric center of the donor glycoside through an S_N2-f-type mechanism. In this process, the diphosphate leaving group of the donor glycoside forms a hydrogen bridge with the incoming nucleophilic alcohol of the acceptor glycoside.

To understand the molecular features that govern the competition between the S_N2-b and S_N2-f reaction pathways, here it is analyzed how the reaction profiles of the S_N2-b and S_N2-f reaction pathways develop for a series of substitution reactions involving phenolic alcohol nucleophiles and alkyl triflate (CH_3OTf, CH_3CH_2OTf, $(CH_3)_2CHOTf$) electrophiles,[43] using density functional theory (DFT; Scheme 2). Phenolic alcohol nucleophiles were selected due to their prominent involvement in S_N2-f pathways, and their tunable hydrogen bond donating properties, as demonstrated in the earlier described solvolysis experiments.[25–34] To analyze the generality of the reactivity trends for these systems, the reaction pathways of a series of partially fluorinated ethanol derivates were also explored.[44,45] The triflate leaving group was chosen as it represents one of the most powerful leaving groups in S_N2 reactions. This study provides a systematic overview of reactivity trends over a wide range of reactivities and pathways. The activation strain model (ASM)[46–48] of reactivity in conjunction with Kohn–Sham molecular orbital (KS-MO) theory[49–51] were employed to pinpoint the physical phenomena that control the competition between the backside and frontside S_N2 pathway of the aforementioned reactions.

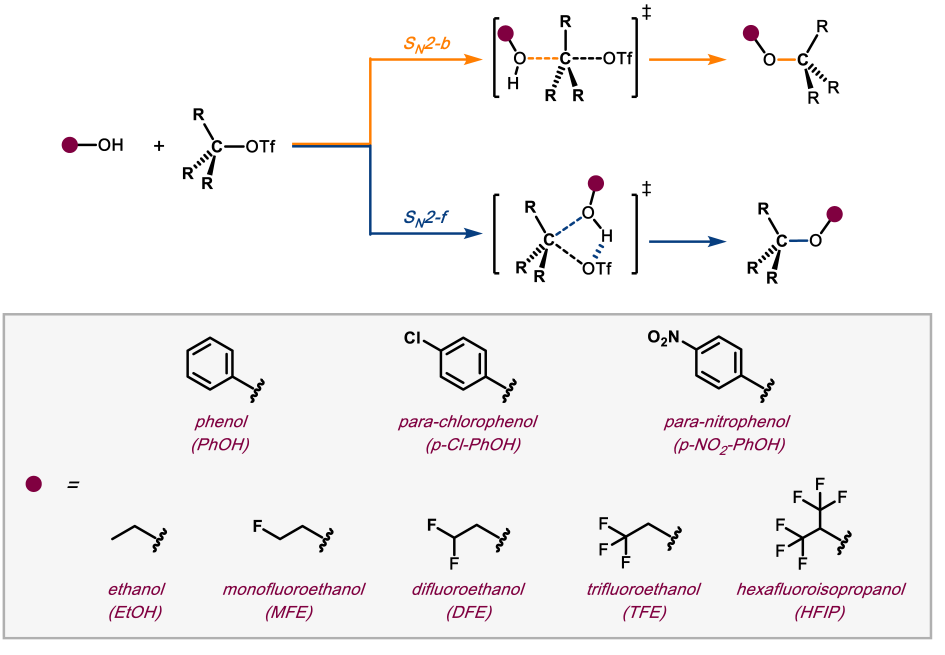

Scheme 2. Schematic overview of the computationally analyzed S_N2-b (orange) and S_N2-f (blue) reactions (R = H or Me).

Results and Discussion

General Trends in Reactivity

The results of the computed reaction profiles of the studied S_N2-b and S_N2-f reactions are collected in Table 1-2 and Figure 1 (see Table S14-S15 for all coordinates).[52] Generally, the reaction proceeds from a reactant complex (RC) through a transition state (TS) towards an intermediate (INT), which eventually dissociates into the products (P). Note, that the overall activation energy ($\Delta E^{\ddagger}$) of the reaction in the gas phase is the energy difference between the TS and the infinitely separated reactants (see, for example, reference 53 and 54 for a more detailed discussion).[55] Representative structures of all stationary points of the reaction profile can be found in Figure S2. Analyzing the structural data of the computed transition states (see Figure 1), it becomes evident that these are relatively 'product-like', which is the direct result of the weak neutral alcohol nucleophiles. The resulting fundamental implications will discussed later in more detail. Importantly, the computed trends in reactivity at ZORA-OLYP/QZ4P agree well with those calculated at the more accurate (TightPNO)DLPNO-CCSD(T)/CBS(3,4/def2)//ZORA-OLYP/QZ4P[56–64] level (see Table S2-S4).

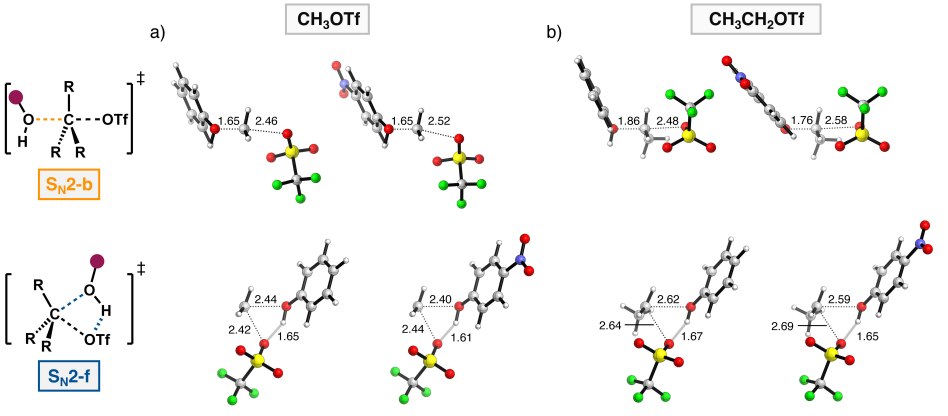

Figure 1. Transition state structures[65] with key bond lengths (in Å) for the S_N2-b and S_N2-f reactions of (a) PhOH (left) and *p*-NO_2-PhOH (right) + CH_3OTf and (b) PhOH (left) and *p*-NO_2-PhOH (right) + CH_3CH_2OTf. Computed at ZORA-OLYP/QZ4P. Atom colors: carbon (gray), hydrogen (white), fluorine (green), nitrogen (blue), oxygen (red), and sulfur (yellow).

Several apparent trends emerge by analyzing the reaction profiles (reactivity trends are consistent for ΔE and ΔG; see SI Table S5-S8). In line with previous findings,[66–71] the activation energy for the S_N2-b increases as the nucleophile becomes less basic (*i.e.*, worse electron-donating capacity), going from PhOH to *p*-Cl-PhOH to *p*-NO_2-PhOH (see Table 1). Typically, the activation energy for the S_N2-f pathway also increases along this series. The increasing activation energy along the phenol series correlates well with the decreasing thermodynamic basicity of the nucleophile going from PhOH to *p*-Cl-PhOH to *p*-NO_2-PhOH. This property is illustrated by the computed proton affinity of these nucleophiles ($\Delta H_{PA} = \Delta H_{ROH} - \Delta H_{RO^-} + \Delta H_{H^+}$; Table S9), which decreases going from ΔH_{PA} = 348.4 (PhOH) to 341.9 (*p*-Cl-PhOH) to 324.7 (*p*-NO_2-PhOH) kcal mol^{-1}, and is in excellent agreement with experimental measurements as well as other computational studies.[72–79]

Table 1. Energies relative to the separated reactants (in kcal mol^{-1}) of the stationary points (RC = reactant complex, TS = transition state, INT = intermediate, and P = product) of the S_N2-b (orange) and S_N2-f (blue) pathways.[a]

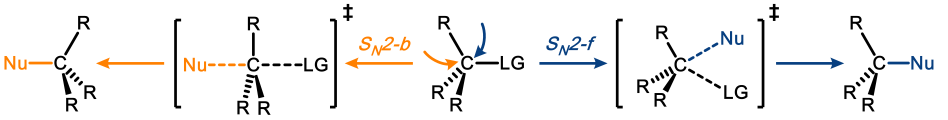

Nucleophile		Electrophile					
		CH_3OTf		CH_3CH_2OTf		$(CH_3)_2CHOTf$	
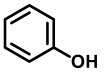	RC[b]	−2.3	[d]	−2.5	[d]	−2.6	(−0.2)
	S_N2-b-TS	42.4	(25.5)	40.3	(27.5)	37.5	(23.1)
	S_N2-f-TS	50.8	(48.8)	41.8	(36.6)	32.2	(23.5)
	INT[c]	−4.3	(−1.1)	−3.2	0.4	−1.1	2.2
	P	0.8	(1.1)	1.4	(3.3)	3.4	(8.8)
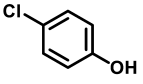	RC[b]	−2.7	(−0.4)	−2.8	(−0.3)	−3.0	(−0.3)
	S_N2-b-TS	44.1	(26.8)	41.7	(28.6)	38.7	(23.6)
	S_N2-f-TS	50.7	(48.6)	41.6	(36.4)	31.8	(23.3)
	INT[c]	−3.9	(−0.9)	−2.9	0.6	−0.9	2.0
	P	0.5	(0.9)	1.1	(1.8)	3.1	(3.5)
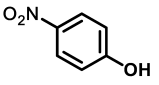	RC[b]	−3.3	(−0.5)	−3.1	(−0.4)	−3.7	(−0.6)
	S_N2-b-TS	49.7	(32.4)	47.0	(31.0)	[e]	[e]
	S_N2-f-TS	54.2	(52.0)	44.2	(38.3)	33.3	(23.6)
	INT[c]	−2.7	0.1	−1.8	[d]	[d]	[d]
	P	0.4	(0.7)	0.8	(1.6)	2.5	(3.0)

[a] Electronic energies computed at the ZORA-OLYP/QZ4P and COSMO(CH_2Cl_2)-ZORA-OLYP/QZ4P in parentheses, relative to infinitely separated reactants. [b] Only the S_N2-f pathway involves a very weakly bound reactant complex RC, the energy of which is provided, while the S_N2-b pathway does not have a stable RC. [c] The product complex of the S_N2-b pathway results in charge separation, inducing a barrierless proton transfer, forming the more stable S_N2-f intermediate (INT). [d] Stationary point is not stable in solution. [e] Transition state cannot be located due to the instability of the associated product.

Table 2. Energies relative to the separated reactants (in kcal mol^{-1}) of the stationary points (RC = reactant complex, TS = transition state, INT = intermediate, and P = product) of the S_N2-b (orange) and S_N2-f (blue) pathways.[a]

Nucleophile		Electrophile					
		CH_3OTf		CH_3CH_2OTf		$(CH_3)_2CHOTf$	
OH	RC[b]	−2.2	[c]	−2.3	[c]	−2.3	[c]
	S_N2-b-TS	35.1	(19.2)	33.9	(22.7)	32.3	(21.5)
	S_N2-f-TS	51.5	(49.2)	43.2	(37.5)	34.8	(24.9)
	INT[c]	−8.4	(−5.6)	−7.1	(−4.0)	−4.7	(−2.0)
	P	−1.9	(−1.3)	−1.1	(−0.5)	2.5	(2.4)
F OH	RC[b]	−1.9	[d]	−1.0	[d]	−2.0	[d]
	S_N2-b-TS	37.2	(22.8)	35.5	(25.3)	33.3	(23.4)
	S_N2-f-TS	52.4	(50.0)	43.3	(37.7)	34.6	(24.7)
	INT[c]	−6.6	(−3.9)	−5.2	(−2.3)	−3.2	(−1.4)
	P	0.9	(1.0)	1.5	(1.6)	3.9	(2.7)
F OH F	RC[b]	−2.2	[d]	−2.4	[d]	−2.2	[d]
	S_N2-b-TS	40.9	(26.0)	38.4	(27.5)	35.6	(25.0)
	S_N2-f-TS	54.1	(51.5)	44.8	(38.7)	35.4	(24.9)
	INT[c]	−5.4	(−2.8)	−4.3	(−1.3)	−2.7	(−0.6)
	P	0.8	(1.0)	1.4	(1.5)	4.1	(2.9)
F F OH F	RC[b]	−2.3	[d]	−1.1	[d]	−1.2	[d]
	S_N2-b-TS	43.8	(24.9)	42.0	(29.2)	38.6	(25.6)
	S_N2-f-TS	54.8	(52.4)	45.0	(39.0)	35.4	(24.9)
	INT[c]	−5.2	(−2.5)	−4.2	(−1.0)	−3.3	(−0.5)
	P	0.5	(0.7)	1.0	(1.1)	2.4	(2.0)
F F F F OH F F	RC[b]	−2.0	[d]	−2.5	(−0.4)	−2.4	(−0.5)
	S_N2-b-TS	50.7	(35.8)	45.7	(34.0)	41.4	(28.8)
	S_N2-f-TS	57.6	(54.7)	46.6	(39.3)	35.6	(25.6)
	INT[c]	−2.9	(−0.7)	−1.8	[d]	−0.4	[d]
	P	0.9	(0.4)	1.0	(0.5)	2.5	(1.7)

[a] Electronic energies computed at the ZORA-OLYP/QZ4P and COSMO(CH_2Cl_2)-ZORA-OLYP/QZ4P in parentheses, relative to infinitely separated reactants. [b] Only the S_N2-f pathway involves a very weakly bound RC, the energy of which is provided, while the S_N2-b pathway does not have a stable RC. [c] Product complex of the S_N2-b pathway results in charge separation, inducing a barrierless proton transfer, forming the more stable S_N2-f intermediate (INT). [d] Stationary point is not stable in solution.

Importantly, in all cases, the activation energy rises significantly more rapidly along this series for the S_N2-b pathway than for S_N2-f. For example, in going from PhOH to *p*-Cl-PhOH to *p*-NO_2-PhOH for CH_3CH_2OTf, the S_N2-b activation energy (S_N2-b-TS in Table 1) increases from $\Delta E^{\ddagger}$ = +40.3 to +41.7 to +47.0 kcal mol^{-1} ($\Delta\Delta E^{\ddagger}$ = +6.7 kcal mol^{-1}), respectively. While the S_N2-f activation energy (S_N2-f-TS in Table 1) rises more moderately from $\Delta E^{\ddagger}$ = +41.8 to +41.6 to +44.2 kcal mol^{-1} ($\Delta\Delta E^{\ddagger}$ = +2.4 kcal mol^{-1}), respectively. Consequently, the preferred reaction pathway switches from S_N2-b for the stronger alcohol nucleophiles to S_N2-f for weaker alcohol nucleophiles. Hence, the S_N2-b prevails for PhOH over the S_N2-f pathway with CH_3CH_2OTf ($\Delta\Delta E^{\ddagger}$ = –1.5 kcal mol^{-1} for the S_N2-b relative to S_N2-f). The S_N2-b and S_N2-f pathways have roughly equal activation energy for *p*-Cl-PhOH ($\Delta\Delta E^{\ddagger}$ = +0.1 kcal mol^{-1} for the S_N2-b relative to S_N2-f), and the S_N2-f pathway dictates the reaction for the least basic *p*-NO_2-PhOH ($\Delta\Delta E^{\ddagger}$ = +2.8 kcal mol^{-1} for the S_N2-b relative to S_N2-f). These reactivity trends are found regardless of the electrophile (CH_3OTf, CH_3CH_2OTf, $(CH_3)_2CHOTf$). Notably, the set of fluorinated ethanol derivates (Table 2; CH_3CH_2OH, CH_2FCH_2OH, CHF_2CH_2OH, CF_3CH_2OH, and $(CF_3)_2CH_2OH$), spanning a large range of reactivities, exhibit exactly the same trend.

The introduction of alkyl-substituents on the electrophile decreases the activation energies for both S_N2 pathways for all the neutral alcohol nucleophiles, which is in line with the experimental[80] and computational[81–83] work of the group of Uggerud. Notably, the decrease in activation energy occurs at a considerably faster rate for the S_N2-f pathway compared to the S_N2-b reactions within the two series. For example, for PhOH as the nucleophile, in going from CH_3OTf to CH_3CH_2OTf to $(CH_3)_2CHOTf$, the S_N2-b activation energy decreases from $\Delta E^{\ddagger}$ = +42.4 to +40.3 to +37.5 kcal mol^{-1} ($\Delta\Delta E^{\ddagger}$ = –4.9 kcal mol^{-1}), respectively. While the S_N2-f activation energy drops steeply from $\Delta E^{\ddagger}$ = +50.8 to +41.8 to +32.2 kcal mol^{-1} ($\Delta\Delta E^{\ddagger}$ = –18.6 kcal mol^{-1}) along the same series. Thus, by the increase of alkyl-substituents on the electrophile, the most prevalent reaction pathway switches from S_N2-b to S_N2-f. This reactivity trend is found irrespective of the nucleophile.

To understand the role of solvation on the studied computed reactivity trends, all reaction profiles were calculated in bulk solution with the use of the conductor-like screening model (COSMO) (Table 1 and 2, data in brackets).[84] It is found that bulk solvation[85] in the studied systems using neutral alcohol nucleophiles, lowers the activation energies of both S_N2 pathways. The solvent stabilizes the developing charges in the transition states, and hence, lowers the overall activation energy. It is noted that this effect is more apparent for the S_N2-b than S_N2-f,[86] resulting from the stabilization of the developing charge in the S_N2-b, in which the leaving group departs as an anion (*e.g.*, TfO^- in the studied systems) and the addition of the nucleophilic alcohol leads to the build-up of positive charge. In contrast, in the S_N2-f pathway, the leaving group is protonated by the incoming nucleophilic alcohol, accommodating the developing charge more within the substitution system.[87]

Activation Strain Analyses

To gain quantitative insight into the factors controlling the reactivity of the S_N2-b and S_N2-f reaction pathways, the activation strain model (ASM) was employed.[46–48] As detailed in the Computational Methods section, the ASM is a fragment-based approach in which the reaction profile can be described with respect to the characteristics of the reactants (alcohol and alkyl triflate). The ASM decomposes the total electronic energy (ΔE) of the system, as found in Table 1 and 2, into two chemically intuitive and useful terms: the destabilizing strain (*i.e.*, distortion energy; ΔE_{strain}) and stabilizing interaction energy (ΔE_{int}) along the reaction, that is: $\Delta E = \Delta E_{strain} + \Delta E_{int}$. This method has proven to be a valuable tool for understanding activation energies, and therefore chemical reactivity.[88–93]

Figure 2 shows how the alcohol nucleophile (panels a and c) and degree of substitution on the electrophile (panels b and d) affect the activation energy of both S_N2-b (top, panel a and b) and S_N2-f (bottom, panel c and d) reaction pathway. Of note, all other combinations of nucleophiles and electrophiles provide similar trends and can be found in Figures S3-S6.

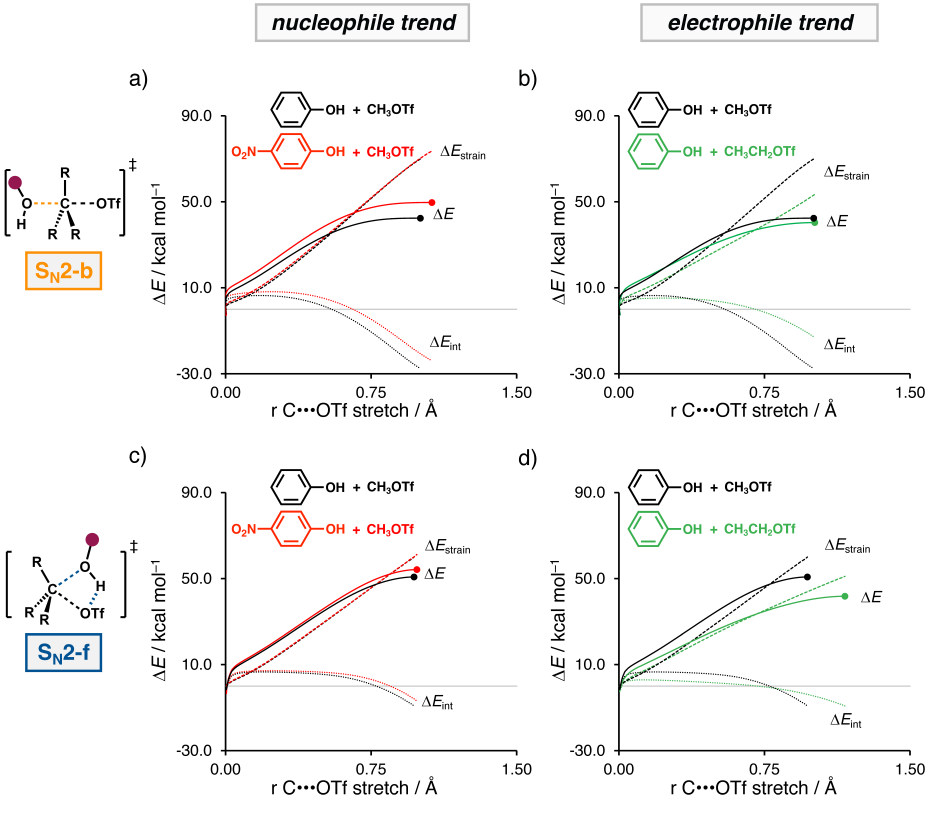

Figure 2. Activation strain analysis of the S_N2-b and S_N2-f reactions along the IRC projected on the C•••OTf bond stretch. The left column (a to c) shows the impact of the nucleophile on the activation energy, whereas the right column (b to d) shows the influence of the degree of electrophile substitution. Transition states are indicated with a thick dot and the zero line with a grey line in the ASD. Computed at ZORA-OLYP/QZ4P.

Decreasing the basicity of the alcohol, by changing from PhOH (black) to *p*-NO_2-PhOH (red) leads to an increase in the activation barrier for both the S_N2-b (Figure 2a) and S_N2-f (Figure 2c). In line with earlier work of Bickelhaupt and co-workers,[66–71] this increase is due to a diminished interaction energy between the nucleophile and the electrophile, as can be gauged from the red interaction energy curve of *p*-NO_2-PhOH, that lies above the black curve of PhOH over the entire course of the reaction. The strain energy is minimally affected by changing the nucleophile.

The weakening of the nucleophile–electrophile interaction can be directly traced back to the electron-withdrawing character of the groups on the nucleophilic alcohol, resulting in a lower-lying (*i.e.*, more stabilized) HOMO going from PhOH to *p*-Cl-PhOH, to *p*-NO_2-PhOH (see Table S10). Thus, weakening the $HOMO_{nucleophile}$–$LUMO_{electrophile}$ orbital interaction (Figure 4a). At the same time, the electron-withdrawing groups also reduce the charge density on the nucleophilic center of the alcohols, weakening the stabilizing electrostatic interactions with the electrophile. This effect is demonstrated in Figure 4c, where the Voronoi deformation density (VDD) atomic charges of the nucleophilic oxygen of the alcohol diminish from –0.181 to –0.163 (see Table S12 for VDD data of all nucleophiles).

Interestingly, the diminished nucleophile–electrophile interaction for weaker alcohol nucleophiles is significantly more pronounced for the S_N2-b than the S_N2-f pathway. Thus, the loss in interaction for weaker alcohol nucleophiles between the nucleophile and electrophile is more evident for the S_N2-b reactions than for the corresponding S_N2-f system. This loss in interaction originates directly from the hydrogen bond between the nucleophile and the leaving group of the electrophile in the S_N2-f pathway, which is not possible in the S_N2-b reaction (Scheme 2). Potentially, this hydrogen bond between the incoming alcohol and the leaving group can enhance the nucleophilicity of the alcohol and assist the leaving group by stabilizing the developing charges along the reaction. This hydrogen bond strengthens when the alcohol nucleophiles become less basic, partly compensating for the loss of the primary $HOMO_{nucleophile}$–$LUMO_{electrophile}$ interaction going from strong to weak nucleophilic alcohols (Figure S7).

Changing the electrophile from CH_3OTf (black) to CH_3CH_2OTf (green) leads to a lowering of both the S_N2-b (Figure 2b) and S_N2-f (Figure 2d) activation energy, originating from a less destabilizing strain energy. This stems from the better leaving group ability of the electrophile as the degree of substitution increases. As reported by Vermeeren *et al.*, this effect stems from the increased steric repulsion between the substituents and the leaving group, effectively weakening and elongating the C–OTf bond (see Table S13 for all data).[94] In contrast, the interaction energy between the nucleophile and the electrophile is less stabilizing for the more substituted electrophiles, which is the direct result of the increasing steric repulsion between the incoming nucleophile and the substituents of the electrophile (Figure S7). However, in the studied systems, this factor is not dominant as a result of the weak neutral alcohol nucleophiles, which engage in a relatively weak nucleophile–electrophile interaction.[95,96] Thus, the activation energy decreases for the more substituted electrophiles because of the weaker carbon–leaving group bond, requiring less destabilizing strain energy to break this bond.

To visualize the competition between S_N2-b and S_N2-f for these systems, Figure 3 presents four panels to describe the S_N2-b/S_N2-f pathways of the reactions: CH_3OTf + PhOH (panel a), CH_3OTf + *p*-NO_2-PhOH (panel b), CH_3CH_2OTf + PhOH (panel c), CH_3CH_2OTf + *p*-NO_2-PhOH (panel d). Thus, in the horizontal direction (a to b and c to d) the effect of the alcohol nucleophile on the reaction energy profile can be inspected, while in the vertical direction (a to c and b to d) the effect of the electrophile becomes apparent. Several characteristic trends for the S_N2-b and S_N2-f pathways can be derived from the computed activation strain diagrams (ASDs).

In line with previous work on the S_N2-b/S_N2-f competition involving anionic X^- + $CH_3Y \rightarrow CH_3X + Y^-$ systems with X and Y = F, Cl, Br, and I,[14–24] it was generally found that the S_N2-b engages in a stronger nucleophile–electrophile interaction. As discussed earlier, this

stronger interaction can be attributed to a more efficient approach of the nucleophile HOMO towards the electrophile LUMO in the S_N2-b pathway because most of the LUMO orbital amplitude is located at the backside of the electrophile. The build-up of stabilizing interaction energy for the S_N2-f occurs later along the reaction coordinate than for the S_N2-b reaction, leading to a weaker nucleophile–electrophile interaction. This delay in interaction energy build-up is the direct result of the more congested nature of the S_N2-f pathway, which requires the carbon–leaving group bond to elongate, to avoid destabilizing steric repulsion before the nucleophile can come closer and engage in a stabilizing bonding overlap with the σ* of the electrophile.

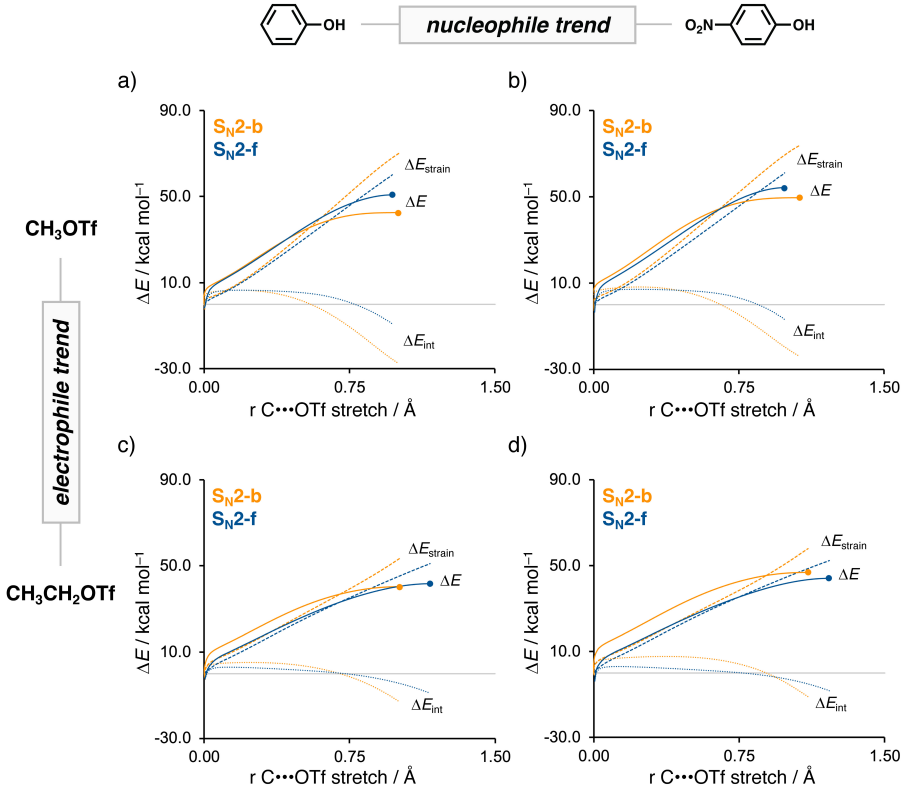

Figure 3. Activation strain analysis of the competition between S_N2-b (orange) and S_N2-f (blue) reactions along the IRC projected on the C•••OTf bond stretch. Trends in the vertical direction (a to c and b to d) show the impact of the degree of substitution of the electrophile, while the trends in the horizontal direction (a to b and c to d) show the influence of the nucleophile. Transition states are indicated with a thick dot and the zero line with a grey line in the ASM diagram. Computed at ZORA-OLYP/QZ4P.

Notably, the trend for the primary $HOMO_{nucleophile}$–$LUMO_{electrophile}$ orbital interaction (Figure 4a) is less pronounced in the overall S_N2-b/S_N2-f competition for these alcohol nucleophiles compared to the previously studied anionic X^- nucleophiles. This trend is less pronounced because the loss of $HOMO_{nucleophile}$–$LUMO_{electrophile}$ interaction energy for weaker alcohols in the S_N2-f pathway is (partly) compensated by a stabilizing hydrogen bond between the nucleophile and the leaving group of the electrophile. As the hydrogen bond becomes stronger for the weaker, and more acidic, alcohol nucleophiles, the S_N2-b/S_N2-f competition shifts from S_N2-b to S_N2-f. The hydrogen bond leads to stabilizing orbital and electrostatic interactions[97,98] between the incoming nucleophile and the leaving group of the electrophile (see Figure 4 and Figure S8). This hydrogen bond interaction has parallels with the findings of Poater *et al.* using counterions in S_N2 reactions ($MX + CH_3Y \rightarrow CH_3X + MY$ with $M^+ = Li^+$, Na^+, K^+, $MgCl^+$).[17] Here, the authors found that the metal counterion M^+ interacts with the leaving group Y to stabilize the S_N2-f pathway.

The orbital interactions for the hydrogen bond stem from the interaction between the lone pair orbitals of the oxygens atoms of the leaving group (*i.e.*, high-lying orbitals, FMOs, including the HOMO) and the σ* orbital of the H–O bond of the alcohol (Figure 4b). This interaction becomes stronger for the weaker alcohols, which have a lower-lying accepting σ* orbital, and thus, a smaller $LUMO_{nucleophile}$–$HOMO_{electrophile}$ orbital energy gap (see Table S11). The stabilizing electrostatic interactions can be traced back to the δ^- of the O-atoms of the leaving group interacting with δ^+ of the H-atom of the alcohol (Figure 4c). This electrostatic interaction is strengthened for the more acidic alcohols, giving rise to more δ^+ character at the H-atom of the alcohol. This trend is illustrated in Figure 4c, where the VDD atomic charges of the H-atom of the alcohol increase from +0.196 to +0.209 (see Table S12 for VDD data of all nucleophiles). In other words, the electron-withdrawing group of the weaker alcohol nucleophiles reduces the electron density on the nucleophilic center, weakening the nucleophile–electrophile interaction for both the S_N2-b and S_N2-f pathway. At the same time, they make the alcohol nucleophiles more acidic, resulting in stronger electrophile–nucleophile interaction for the S_N2-f pathway, which is not available for the S_N2-b reaction.

For the studied systems, the S_N2-f pathway always proceeds with less destabilizing strain energy than its S_N2-b counterpart (Figure 3), which can be explained by the lack of the Walden inversion along the S_N2-f pathway. This result is in contrast with the findings of Bickelhaupt and co-workers.[14,15] They investigated the S_N2-b and S_N2-f reactions of $X^- + CH_3Y$, finding that the destabilizing strain energy of the S_N2-f pathway in all cases is more destabilizing than that of the S_N2-b pathway. This result was attributed to the repulsion between the anionic X- and Y-groups in the frontside pathway, causing more deformation of the electrophile.[99,100] In the systems studied here, the repulsion between the incoming nucleophile and electrophile is less pronounced because of the non-charged nucleophile and the development of a stabilizing hydrogen bond between the incoming alcohol nucleophile and the leaving group.

The introduction of alkyl-substituents on the electrophile leads to a shift from an interaction-controlled to a strain-controlled regime. For CH_3OTf, the nucleophile can engage in a strong interaction with the electrophile and favors the S_N2-b due to the intrinsically more efficient approach of the nucleophile HOMO towards the electrophile LUMO. Going to more substituted systems, the primary nucleophile–electrophile interaction diminishes due to the steric repulsion between the reactants, and therefore the system becomes strain-controlled. As mentioned above, for the herein studied systems, the S_N2-f goes with less destabilizing strain energy, and thus, shifts the preference for S_N2-b to S_N2-f. Note that, for the more substituted systems, the S_N2-f pathway even goes with more stabilizing interaction energy in the initial phase of the reaction owing to the presence of the hydrogen bonding interaction.

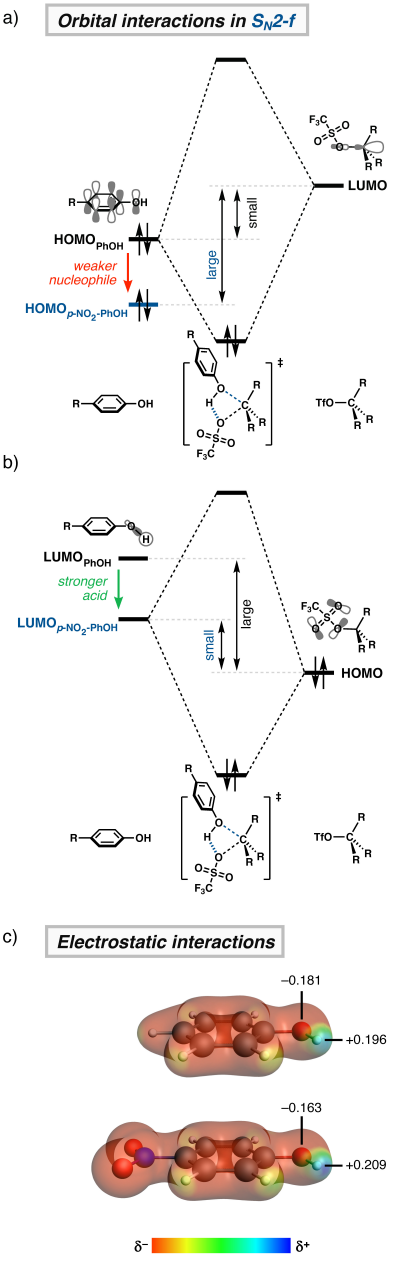

Figure 4. Schematic molecular orbital diagram for the S_N2-f pathway of the most important (a) $HOMO_{nucleophile}$–$LUMO_{electrohile}$ and (b) $LUMO_{nucleophile}$–$HOMO_{electrophile}$ hydrogen bonding interaction. (c) Electrostatic interactions derived from molecular electrostatic potential maps (at 0.03 $Bohr^{-3/2}$) from +0.2 (red) to +0.5 (blue) Hartree e^{-1} and the Voronoi deformation density[101] of the nucleophilic center at their equilibrium geometries. Computed at ZORA-OLYP/QZ4P.

Conclusions

The competition between backside and frontside S_N2 nucleophilic substitution reactions (S_N2-b and S_N2-f) of neutral alcohol nucleophiles with alkyl triflates was studied. Both substitution reactions are slowed when the basicity of the alcohol decreases (*i.e.*, worse electron-donating capacity). However, the S_N2-b pathway slows down more rapidly than the corresponding S_N2-f reactions for the studied series of phenol and fluorinated ethanol nucleophiles. As a result, in going from strong to weak alcohol nucleophiles, the preference for the S_N2-b pathway slowly erodes and the unusual S_N2-f can become most favorable.

Using the activation strain model, the physical factors that govern these reactivity trends were investigated. The higher activation energies for the S_N2-b and S_N2-f substitution reactions of the weaker alcohols can be traced to the weakening of the primary nucleophile–electrophile interaction between the alcohol nucleophile and the electrophile. Importantly, the overall loss in interaction for the weaker alcohol nucleophiles with the electrophiles in the S_N2-f reactions is less apparent than for the corresponding S_N2-b system. This difference is caused by the hydrogen bond between the nucleophile and the leaving group of the electrophile. This hydrogen bond develops along the reaction coordinate in the S_N2-f pathway, an interaction that is not possible in the S_N2-b reaction.

The hydrogen bond strengthens when the alcohol becomes more acidic, compensating for the loss of the primary nucleophile–electrophile interaction going from strong to weaker alcohols. This favorable interaction makes the frontside substitution reactions more favorable for the most acidic nucleophiles, especially in combination with electrophiles that allow for the accumulation of significant positive charge by lengthening the carbon–leaving group bond. It is envisioned that these findings extend well beyond the systems studied here, aiding in understanding the S_N2-b/S_N2-f competition better and designing more effective substitution reactions.

Supporting information

Computational Methods

General Computational Methods

All calculations have been carried out using the Amsterdam Density Functional (ADF; ADF2018.105) software package.[102,102–104] Geometries were optimized at ZORA-OLYP/QZ4P.[105–108] In previous benchmark studies, Bickelhaupt and co-worker have shown that OLYP reproduces S_N2 barriers from highly correlated *ab initio* within only a few kcal mol^{-1}.[109–112] Relativistic effects were accounted for by using the zeroth-order regular approximation (ZORA).[108] The basis set used, denoted QZ4P, can be described as core triple-ζ, valence quadruple-ζ, with four sets of polarization functions.[107] The accuracies of the fit scheme (Zlm fit) and the integration grid (Becke grid) were, for all calculations, set to VERYGOOD.[113,114] All stationary points were confirmed by vibrational analysis: for equilibrium structures, all normal modes have real frequencies, whereas transition states have one normal mode with an imaginary frequency. The optimized structures were illustrated using CYLview.[65] The reaction pathway, towards both the reactant complex and the product complex/intermediate, of the studied substitution reactions were obtained by performing intrinsic reaction coordinate (IRC) calculations,[115–117] which, in turn, were analyzed using the PyFrag program.[118] To account for bulk solvation the conductor-like screening model (COSMO) was used.[119–122] The electronic energies of all stationary points were ,for reference purposes, re-computed at COSMO(CH_2Cl_2)-ZORA-OLYP//ZORA-OLYP/QZ4P, (TightPNO)DLPNO-CCSD(T)/CBS(3,4/def2)//ZORA-OLYP/QZ4P//ZORA-OLYP/QZ4P and SMD(CH_2Cl_2)-(TightPNO)DLPNO-CCSD(T)/CBS(3,4/def2)//ZORA-OLYP/QZ4P. The DLPNO-CCSD(T)[56–62] computations were carried out using ORCA5.04.[63,64]

Thermochemistry

For the thermochemistry calculations, a standard approach was used whereby the geometries were optimized, and the vibrational frequencies were obtained through numerical differentiation of the analytical gradient. Enthalpies at 298.15 K and 1 atm (ΔH) were calculated from the electronic bond energies and vibrational frequencies by using a standard thermochemistry relation for an ideal gas [Eq. S1].

$$\Delta H = \Delta E_{\text{trans}} + \Delta E_{\text{rot}} + \Delta E_{\text{vib},0} + \Delta(\Delta E_{\text{vib},298}) + \Delta(pV) \tag{S1}$$

$\Delta E_{\text{trans},298}$, $\Delta E_{\text{rot},298}$, and $\Delta E_{\text{vib},0}$ are the differences between the reactants in the translational, rotational, and zero-point vibrational energy, respectively, whereas $\Delta E_{\text{vib},298}$ takes the vibrational energy change upon going from 0 to 298.15 K into account. When COSMO was used, entropies were corrected according to the approach of Martin-Hay-Pratt.[123–125] This correction is important because the ideal gas approximation ignores the solvent suppression effect on the rotational and translational degrees of freedom of the solute, which can lead to a large overestimation of the entropy contributions to the Gibbs free energy in solution. In the specific case of bimolecular reactions occurring in dichloromethane at 298.15 K, as in this study, this correction amounts to –3.52 kcal mol^{-1} for all TSs, RCs, and INTs. Finally, the change of the Gibbs free energy (ΔG) in solution was then calculated according to Eq. S2.

$$\Delta G = \Delta H - T\Delta S \tag{S2}$$

Activation Strain Model

The activation strain model of chemical reactivity, also known as the distortion/interaction model, is a fragment-based approach in which the reaction profiles can be described with respect to, and understood in terms of the characteristics of, the reactants. It considers the rigidity of the reactants and to which extent they need to deform during the reaction, plus their capability to interact with each other as the reaction proceeds. With the help of this model, the total energy, *i.e.,* $\Delta E(\zeta)$, is decomposed into the strain and interaction energy, $\Delta E_{\text{strain}}(\zeta)$ and $\Delta E_{\text{int}}(\zeta)$, respectively, and project these values onto the reaction coordinate ζ [Eq. (S3)].

$$\Delta E(\zeta) = \Delta E_{\text{strain}}(\zeta) + \Delta E_{\text{int}}(\zeta) \tag{S3}$$

In this equation, the strain energy, $\Delta E_{\text{strain}}(\zeta)$, is the penalty that needs to be paid to deform the reactants from their equilibrium to the geometry they adopt during the reaction at the point ζ of the reaction coordinate. On the other hand, the interaction energy, $\Delta E_{\text{int}}(\zeta)$, accounts for all the chemical interactions that occur between these two deformed reactants along the reaction coordinate. The total strain energy can, in turn, be further decomposed into the strain energies corresponding to the deformation of the nucleophile, $\Delta E_{\text{strain,nuclehopile}}(\zeta)$, as well as from the electrophile, $\Delta E_{\text{strain,electrophile}}(\zeta)$ [Eq. S4].

$$\Delta E_{\text{strain}}(\zeta) = \Delta E_{\text{strain,nucleophile}}(\zeta) + \Delta E_{\text{strain,electrophile}}(\zeta) \tag{S4}$$

In the herein presented activation strain and accompanied energy decomposition diagrams, the intrinsic reaction coordinate (IRC) is projected onto the carbon–leaving group (C•••OTf) stretch. This critical reaction coordinate undergoes a well-defined change during the reaction from the reactant complex via the transition state to the product and is shown to be a valid reaction coordinate for studying bimolecular reactions. The ASM has been used to analyze the factors affecting the reaction paths of cycloaddition reactions, nucleophilic substitution reactions, eliminations reactions as well as epoxide opening reactions.[66,68,93,126,127]

Energy Decomposition Analysis

The interaction energy, *i.e.,* $\Delta E_{\text{int}}(\zeta)$, between the deformed reactants can be further analyzed in terms of quantitative Kohn-Sham molecular orbital (KS-MO) theory together with a canonical energy decomposition analysis (EDA).[50,51] The EDA decomposes the $\Delta E_{\text{int}}(\zeta)$ into the following three energy terms [Eq. S5].

$$\Delta E_{\text{int}}(\zeta) = \Delta V_{\text{elstat}}(\zeta) + \Delta E_{\text{Pauli}}(\zeta) + \Delta E_{\text{oi}}(\zeta) \tag{S5}$$

Herein, $\Delta V_{\text{elstat}}(\zeta)$ is the classical electrostatic interaction between the unperturbed charge distributions of the (deformed) reactants and is usually attractive. The Pauli repulsion, $\Delta E_{\text{Pauli}}(\zeta)$, includes the destabilizing interaction between the fully occupied orbitals of both fragments due to the Pauli principle. The orbital interaction energy, $\Delta E_{\text{oi}}(\zeta)$, accounts for, amongst others, charge transfer between the fragments, such as HOMO–LUMO interactions.

Proton Affinity

Proton affinities (PA), are calculated at 298.15 K and 1 atm (ΔH_{PA}) from electronic bond energies (ΔE) and vibrational frequencies using standard thermochemistry relations for an ideal gas [Eq. S6].[128,129]

$$\Delta H_{\text{PA}} = \Delta E + \Delta E_{\text{trans},298} + \Delta E_{\text{rot},298} + \Delta E_{\text{vib},0} + \Delta(\Delta E_{\text{vib},0})_{298} + \Delta(pV) \quad \text{(S6)}$$

Here, $\Delta E_{\text{trans},298}$, $\Delta E_{\text{rot},298}$, and $\Delta E_{\text{vib},0}$ are the differences between the alcohol (*i.e.*, ROH) and the separated alkoxide and proton species (*i.e.*, $H^+ + RO^-$; the proton and the alkoxide) in translational, rotational, and zero-point vibrational energy, respectively. The last term, $\Delta(\Delta E_{\text{vib},0})_{298}$, is the change in the vibrational energy difference when going from 0 to 298.15 K. The molar work term $\Delta(pV)$ is $(\Delta n)RT$, where Δn = +1, for one alcohol dissociating into two separate species, namely the H^+ and the alkoxide.

Voronoi Deformation Density

The atomic charge distribution was analyzed by using the Voronoi Deformation Density (VDD) method.[101] The VDD method partitions the space into so-called Voronoi cells, which are non-overlapping regions of space that are closer to nucleus A than to any other nucleus. The charge distribution is determined by taking a fictitious promolecule as reference point, in which the electron density is simply the superposition of the atomic densities of all atoms A [Eq. (S7)]:

$$\rho_{\text{promolecule}}(\text{r}) = \sum_{\text{A}} \rho_{\text{A}}(\text{r}) \quad \text{(S7)}$$

The change in density in the Voronoi cell when going from this promolecule to the final molecular density $\rho(\text{r})$ of the interacting system is associated with the VDD atomic charge Q. The VDD atomic charge Q_A of atom A is calculated according to [Eq. (S8)].

$$Q_{\text{A}}^{\text{VDD}} = -\int_{\text{Voronoi cell of A}} [\rho(r) - \rho_{\text{promolecule}}(\text{r})]d\text{r} \quad \text{(S8)}$$

So, instead of computing the amount of charge contained in an atomic volume, the flow of charge from one atom to the other upon formation of the molecule is computed. The physical interpretation is therefore straightforward. A positive atomic charge Q_A corresponds to the loss of electrons, whereas a negative atomic charge Q_A is associated with the gain of electrons in the Voronoi cell of atom A.

Projecting ill-defined reaction paths onto well-defined reaction paths.

For two of the computed systems (2,2,2-trifluoroethanol–$(CH_3)_2$CHOTf and 1,1,1,3,3,3-hexafluoro-2-propanol–$(CH_3)_2$CHOTf), an S_N2-f transition state could not be established within the specific computational method. To provide some quantitative insight into these reactions, these nucleophiles were projected onto the reaction path (as obtained from the IRC and used in the ASM) of the S_N2-f reaction of 2,2-difluoroethanol with $(CH_3)_2CH_2$OTf. To this end, all 200 geometries of this reaction path were altered to represent either 2,2,2-trifluoroethanol or 1,1,1,3,3,3-hexafluoro-2-propanol. Subsequently, these geometries were partially optimized with freeze constraints on the leaving group, the electrophile, and the nucleophilic OH-group. In other words, for 2,2,2-trifluoroethanol, only the CH_2CF_3 part was optimized, and for 1,1,1,3,3,3-hexafluoro-2-propanol, only the (CF_3)CH part was optimized. The maxima of these *pseudo*-reaction paths were considered to be the transition states. The entire *pseudo*-reaction paths were used for further ASM analysis.

Supplementary Figures and Tables

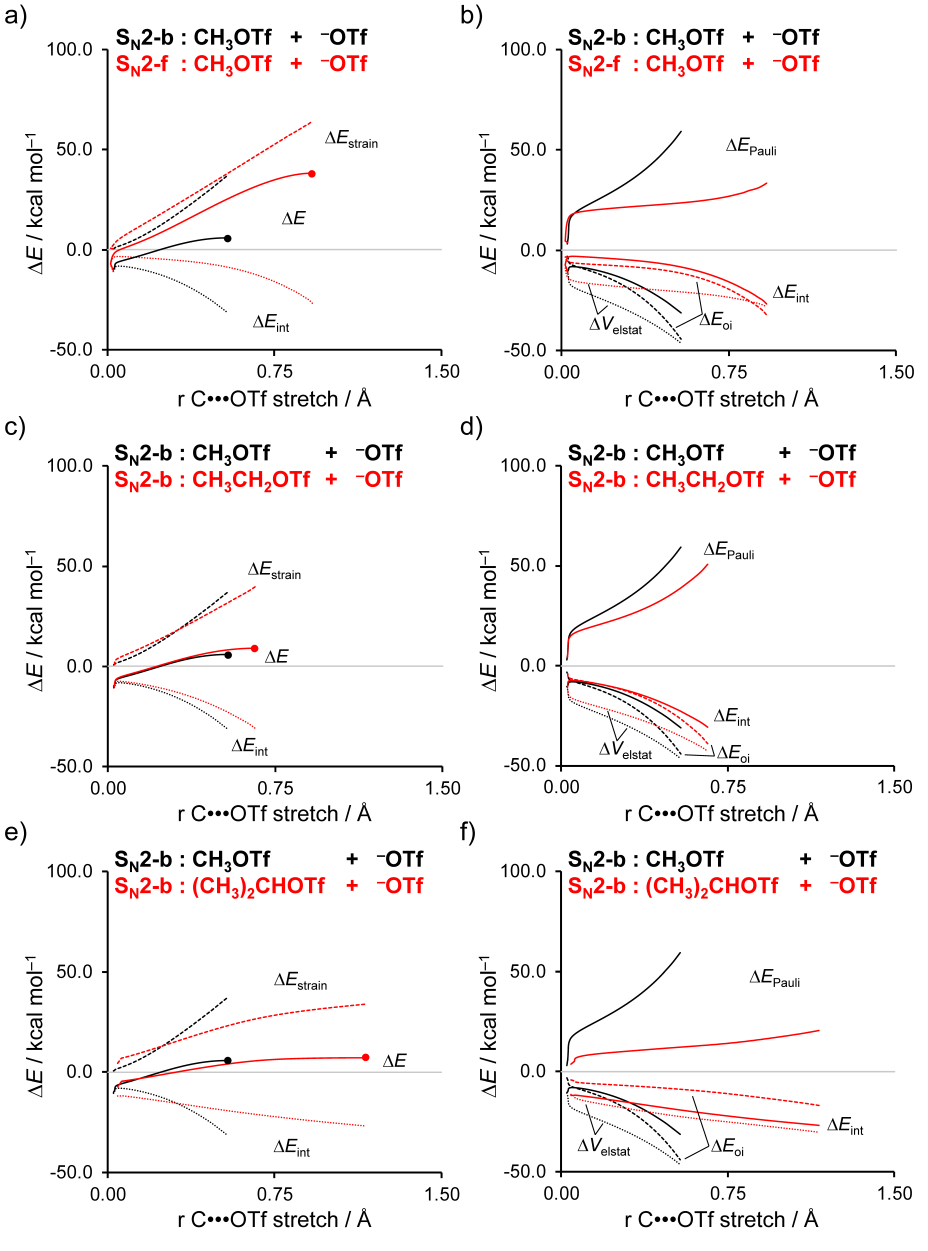

Supplementary Figure S1. Activation strain analysis and energy decomposition analysis of the S_N2-b triflate inversions of CH_3OTf (a-f), CH_3CH_2OTf and $(CH_3)CHOTf$ (c, d), and the S_N2-f triflate inversions of CH_3OTf (a, b), along the IRC projected on the C•••OTf bond stretch. All plots show one of the above-mentioned transition states compared with the S_N2-b triflate inversions of CH_3OTf. Transition states are indicated with a thick dot and the zero line with a grey line in the ASM diagram. Computed at ZORA-OLYP/QZ4P.

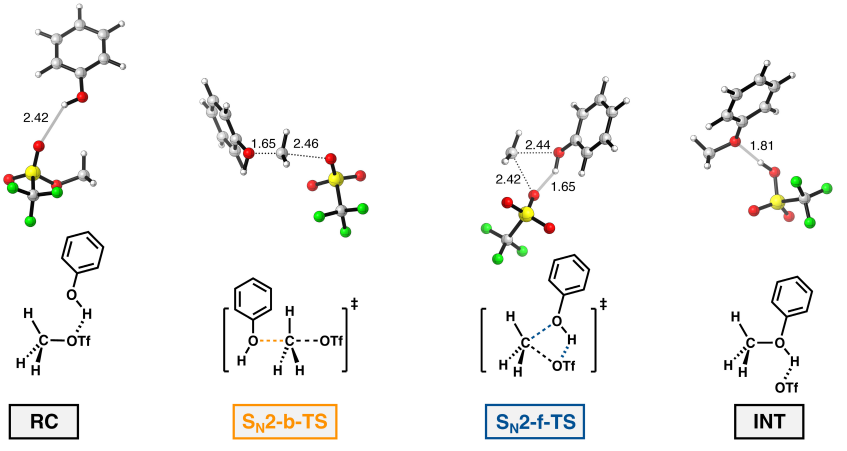

Supplementary Figure S2. Stationary points for the S_N2-b and S_N2-f reactions of PhOH + CH_3OTf. RC = reactant complex, S_N2-b-TS = backside transition state, S_N2-f-TS = frontside transition state, INT = intermediate, and P = product) of the S_N2-b (orange) and S_N2-f (blue) pathways.[Fout! Bladwijzer niet gedefinieerd.] Only the S_N2-f pathway involves a very weakly bound reactant complex RC, while the S_N2-b pathway does not have a stable RC. The product complex of the S_N2-b pathway results in charge separation, inducing a barrierless proton transfer, forming the more stable S_N2-f intermediate.

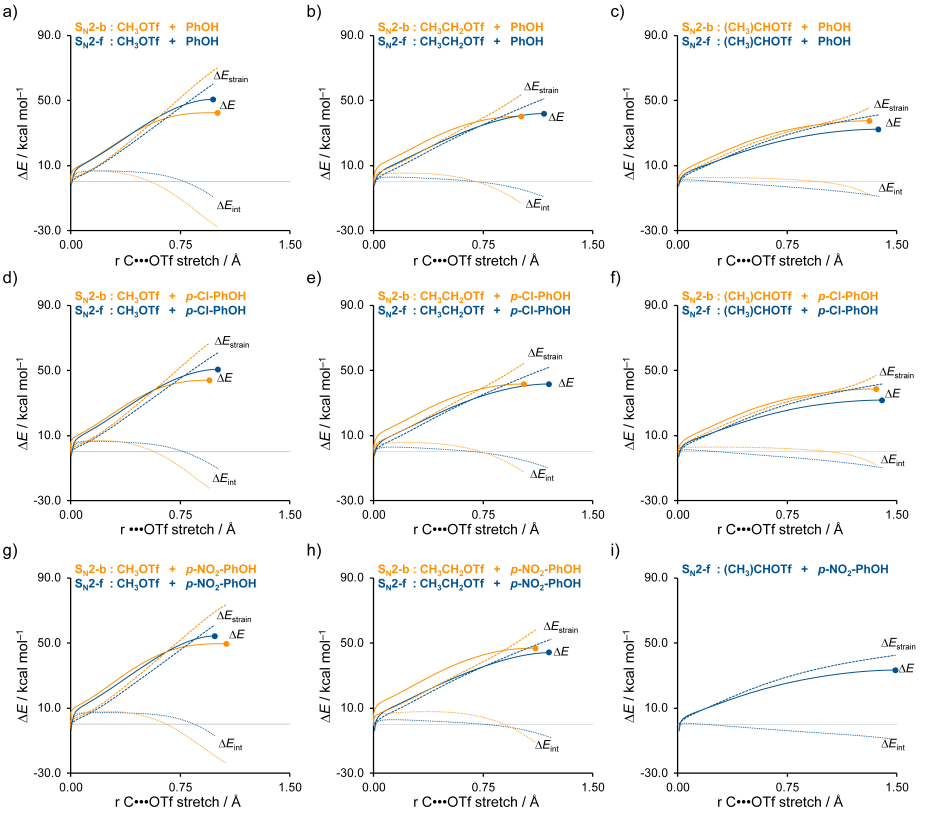

Supplementary Figure S3. Activation strain analysis of the competition between S_N2-b (orange) and S_N2-f (blue) reactions of phenol(-derivates) with CH_3OTf, CH_3CH_2OTf and $(CH_3)CHOTf$ along the IRC projected on the C•••OTf bond stretch. Trends in the vertical direction (a to d to g, b to e to f, and c to f to i) show the influence of the nucleophile on this competition, whereas trends in the horizontal direction (a to b to c, d to e to f, and g to h to i) the impact of the degree of substitution on the electrophile. Transition states are indicated with a thick dot and the zero line with a grey line in the ASM diagram. Computed at ZORA-OLYP/QZ4P.

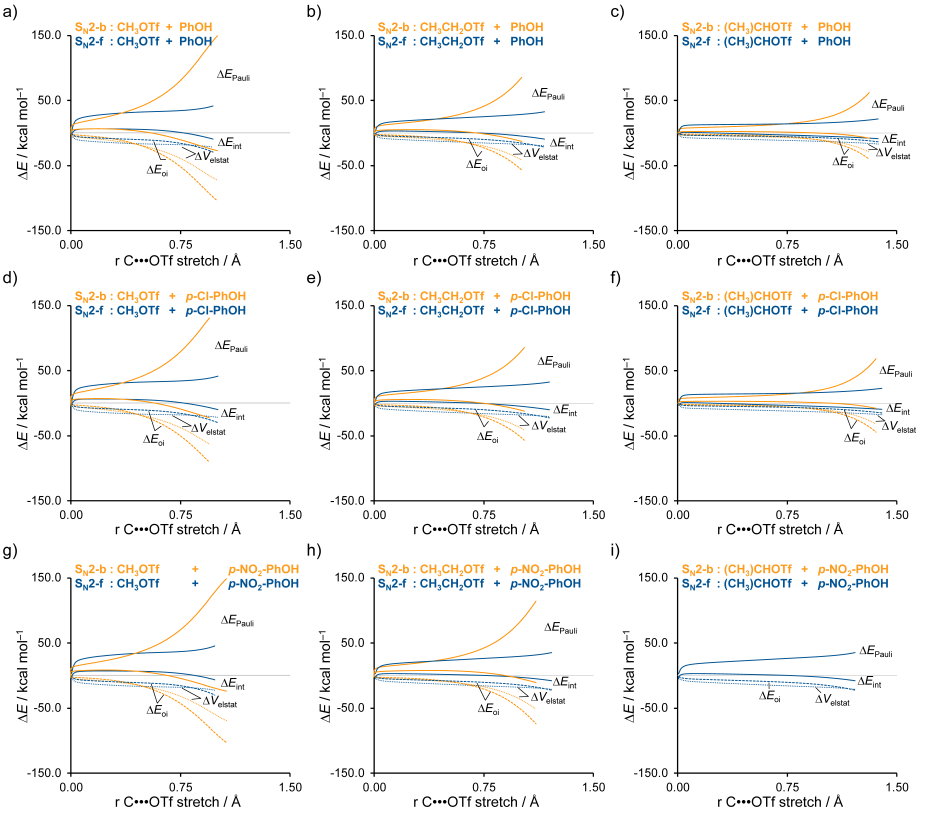

Supplementary Figure S4. Energy decomposition analysis of the competition between S_N2-b (orange) and S_N2-f (blue) reactions of phenol(-derivates) with CH_3OTf, CH_3CH_2OTf and $(CH_3)CHOTf$ along the IRC projected on the C•••OTf bond stretch. Trends in the vertical direction (a to d to g, b to e to f, and c to f to i) show the influence of the nucleophile on this competition, whereas trends in the horizontal direction (a to b to c, d to e to f, and g to h to i) the impact of the degree of substitution on the electrophile. The zero line is indicated with a grey line in the EDA diagram. Computed at ZORA-OLYP/QZ4P.

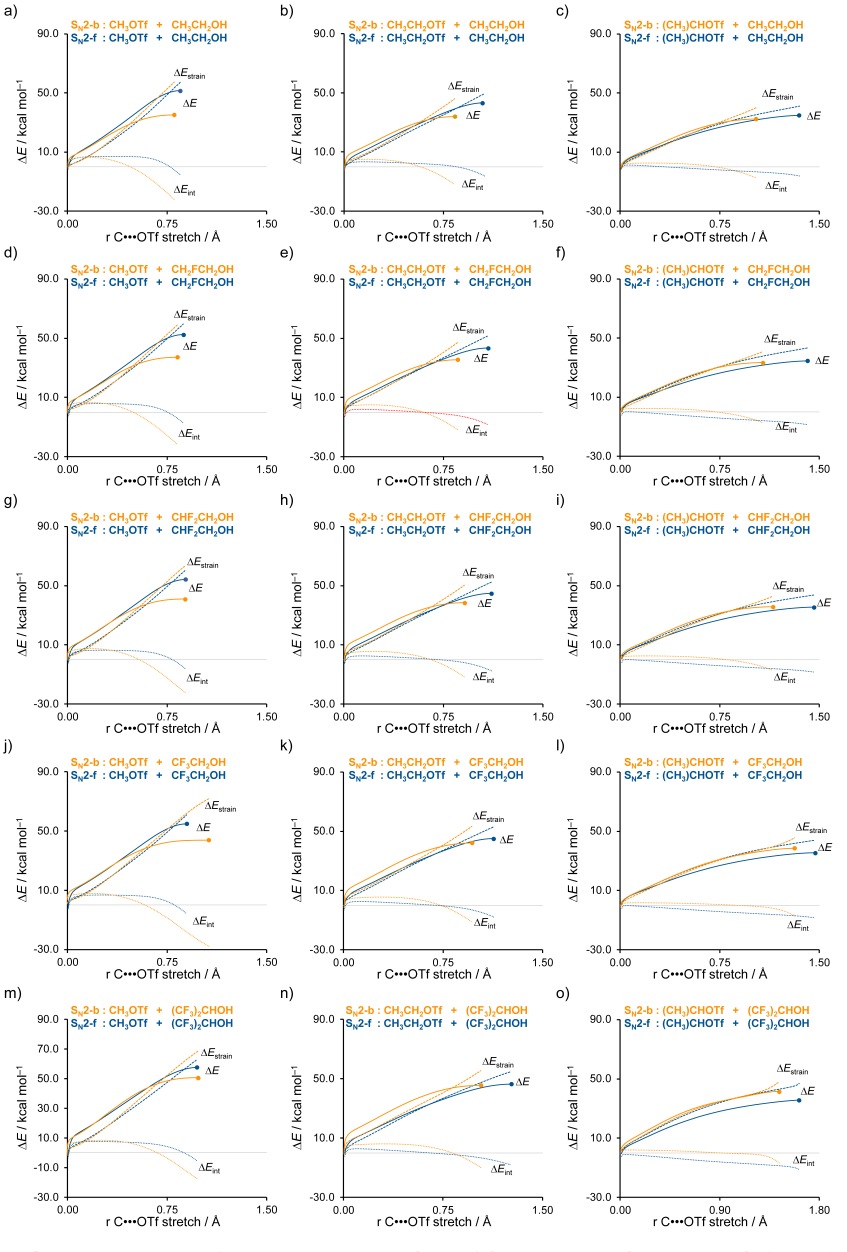

Supplementary Figure S5. Activation strain analysis of the competition between S_N2-b (orange) and S_N2-f (blue) reactions of ethanol(-derivates) with CH_3OTf, CH_3CH_2OTf and $(CH_3)CHOTf$ along the IRC projected on the C•••OTf bond stretch. Trends in the vertical direction (a to d to g to j to m, b to e to h to k to n and c to f to i to l to o) show the influence of the nucleophile, whereas trends in the horizontal direction (a to b to c, d to e to f, and g to h to i, j to k to l and m to n to o) show the impact of the degree of substitution on the electrophile on this competition. Transition states are indicated with a thick dot and the zero line with a grey line in the ASM diagram. Computed at ZORA-OLYP/QZ4P.

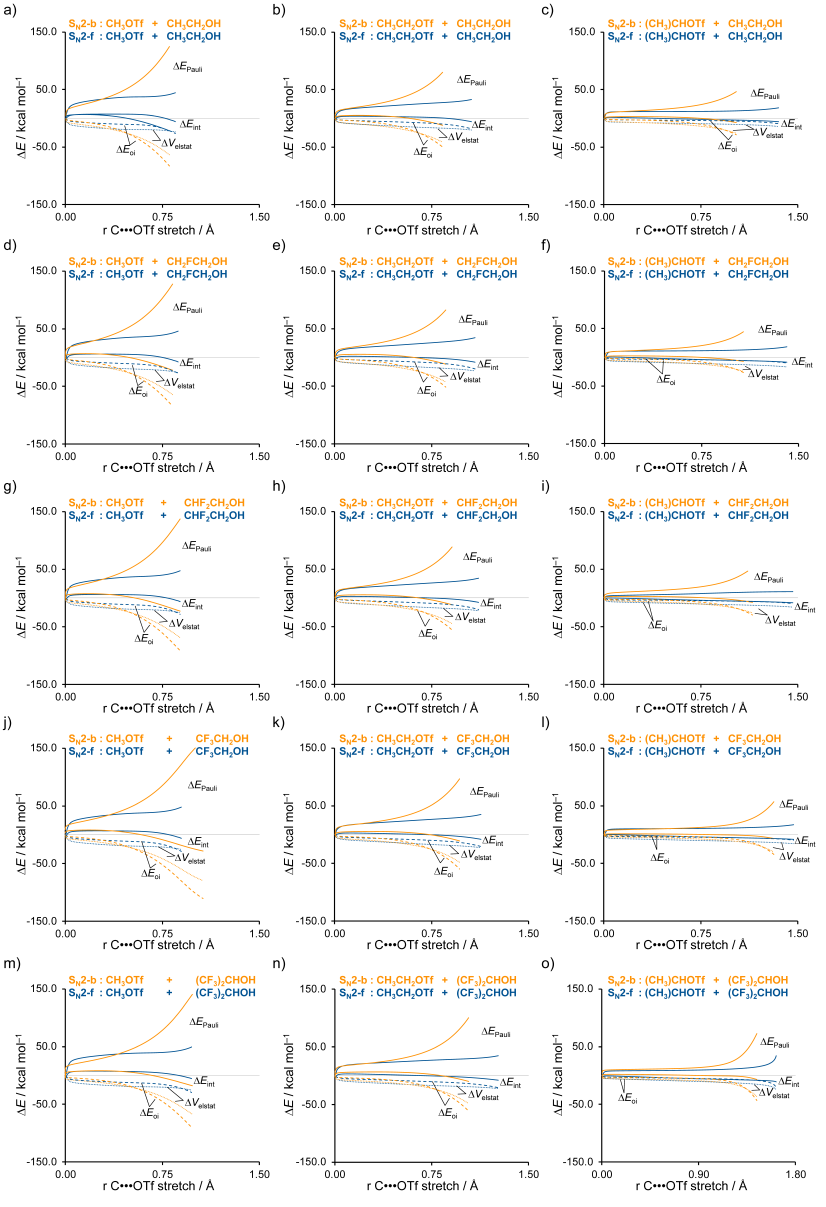

Supplementary Figure S6. Energy decomposition analysis of the competition between S_N2-b (orange) and S_N2-f (blue) reactions of ethanol(-derivates) with CH_3OTf, CH_3CH_2OTf and $(CH_3)CHOTf$ along the IRC projected on the C•••OTf bond stretch. Trends in the vertical direction (a to d to g to j to m, b to e to h to k to n and c to f to i to l to o) show the influence of the nucleophile, whereas trends in the horizontal direction (a to b to c, d to e to f, and g to h to i, j to k to l and m to n to o) show the impact of the degree of substitution on the electrophile on this competition. The zero line is indicated with a grey line in the EDA diagram. Computed at ZORA-OLYP/QZ4P.

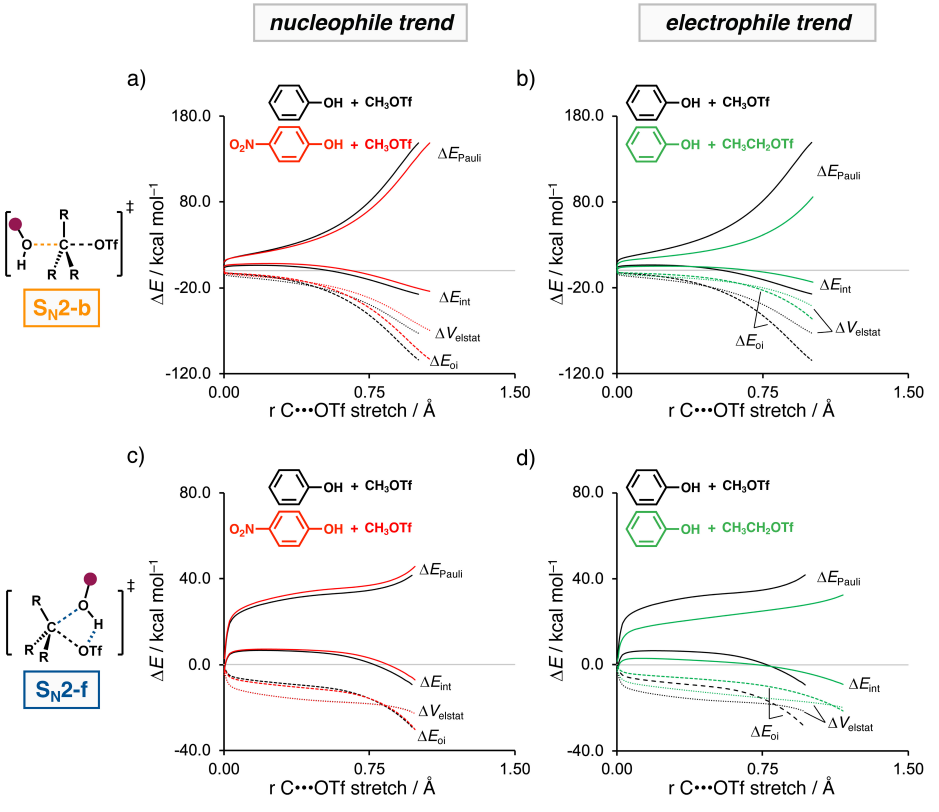

Supplementary Figure S7. Energy decomposition analysis of the S_N2-b and S_N2-f reactions along the IRC projected on the C•••OTf bond stretch. The left column (a to c) shows the impact of the nucleophile on the activation energy, whereas the right column (b to d) shows the influence of the degree of substitution on the electrophile. The zero line is indicated with a grey line in the EDA diagram. Computed at ZORA-OLYP/QZ4P.

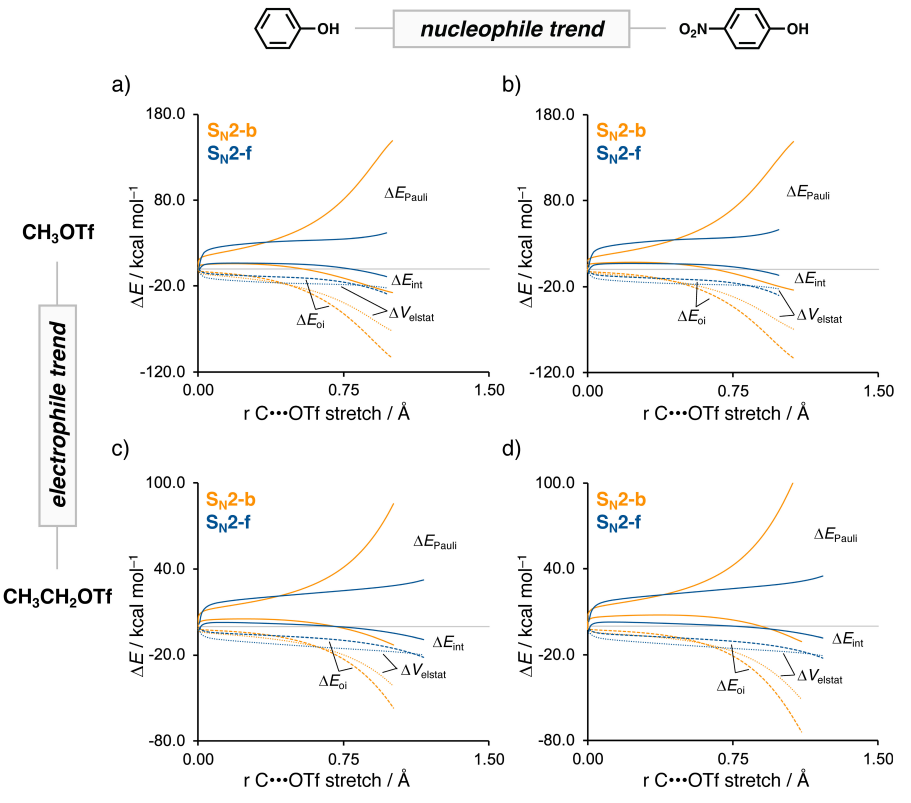

Supplementary Figure S8. Energy decomposition analysis of the competition between S_N2-b (orange) and S_N2-f (blue) reactions along the IRC projected on the C•••OTf bond stretch. Trends in the vertical direction (a to c and b to d) show the impact of the degree of substitution on the electrophile on this competition, whereas trends in the horizontal direction (a to b and c to d) show the influence of the nucleophile. The zero line is indicated with a grey line in the EDA diagram. Computed at ZORA-OLYP/QZ4P.

Supplementary Table S1. Energies relative to the separate reactants (in kcal mol^{-1}) of the transition states (TS) of the S_N2-b and S_N2-f pathways.[a–d]

Nucleophile		Electrophile		
		CH_3OTf	CH_3CH_2OTf	$(CH_3)_2CHOTf$
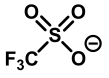	S_N2-b-TS[a] (OLYP)	5.9	9.0	7.2
	S_N2-f-TS[a] (OLYP)	38.2	[e]	[e]
	S_N2-b-TS[b] (COSMO-OLYP)	22.1	23.8	19.1
	S_N2-f-TS[b] (COSMO-OLYP)	50.5	[e]	[e]
	S_N2-b-TS[c] (DLPNO-CCSD(T))	1.4	4.1	8.0
	S_N2-f-TS[c] (DLPNO-CCSD(T))	41.9	[e]	[e]
	S_N2-b-TS[d] (SMD-DLPNO-CCSD(T))	15.1	16.8	17.2
	S_N2-f-TS[d] (SMD-DLPNO-CCSD(T))	48.7	[e]	[e]

[a] Electronic energies computed at ZORA-OLYP/QZ4P. [b] Electronic energies computed at COSMO(CH_2Cl_2)-ZORA-OLYP//ZORA-OLYP/QZ4P. [c] Electronic energies computed at (TightPNO)DLPNO-CCSD(T)/CBS(3,4/def2)//ZORA-OLYP/QZ4P. [d] Electronic energies computed at SMD(CH_2Cl_2)-(TightPNO)DLPNO-CCSD(T)/CBS(3,4/def2)//ZORA-OLYP/QZ4P. [e] Transition state could not be located.

Supplementary Table S2. Energies relative to the separate reactants (in kcal mol^{-1}) of the stationary points (RC = reactant complex, TS = transition state, INT = intermediate, and P = product) of the S_N2-b and S_N2-f pathways.[a]

Nucleophile		Electrophile		
		CH_3OTf	CH_3CH_2OTf	$(CH_3)_2CHOTf$
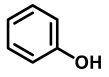	RC[b]	−4.4	−4.8	−5.0
	S_N2-b-TS	32.9	33.1	31.4
	S_N2-f-TS	56.0	45.9	35.8
	INT[c]	−10.9	−10.4	−8.5
	P	1.0	2.8	8.4
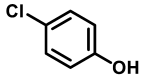	RC[b]	−4.6	−4.7	−5.2
	S_N2-b-TS	34.7	34.5	32.3
	S_N2-f-TS	57.5	46.6	36.1
	INT[c]	−10.3	−9.8	−8.3
	P	0.8	1.9	3.9
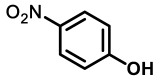	RC[b]	−5.4	−5.9	−6.2
	S_N2-b-TS	39.4	36.6	[d]
	S_N2-f-TS	57.9	46.3	35.9
	INT[c]	−8.4	−7.5	−5.5
	P	0.8	1.9	3.6
	RC[b]	−4.2	−4.3	−4.3
	S_N2-b-TS	27.4	27.2	28.0
	S_N2-f-TS	54.4	45.4	38.1
	INT[c]	−14.4	−13.7	−13.9
	P	−0.4	0.3	3.6
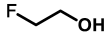	RC[b]	−1.6	−3.1	−4.3
	S_N2-b-TS	28.4	27.9	28.5
	S_N2-f-TS	53.9	44.0	37.0
	INT[c]	−12.2	−11.5	−9.1
	P	2.2	2.9	5.4
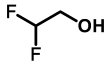	RC[b]	−4.2	−4.5	−4.5
	S_N2-b-TS	31.7	30.6	30.6
	S_N2-f-TS	56.0	45.7	38.0
	INT[c]	−10.7	−10.2	−8.1
	P	2.0	2.6	5.7
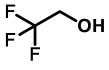	RC[b]	−4.0	−3.5	−3.3
	S_N2-b-TS	34.9	34.3	33.7
	S_N2-f-TS	56.8	45.9	38.0
	INT[c]	−10.3	−9.9	−8.8
	P	1.8	2.3	3.6
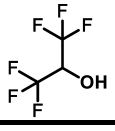	RC[b]	−4.2	−4.8	−4.7
	S_N2-b-TS	41.4	37.4	35.5
	S_N2-f-TS	58.6	46.1	34.2
	INT[c]	−7.2	−5.0	−4.3
	P	1.9	2.0	3.0

[a] Electronic energies computed at (TightPNO)DLPNO-CCSD(T)/CBS(3,4/def2)//ZORA-OLYP/QZ4P. [b] Only the S_N2-f pathway involves a very weakly bound reactant complex RC, the energy of which is provided, while the S_N2-b pathway does not have a stable RC. [c] The product complex of the S_N2-b pathway results in charge separation, inducing a barrierless proton transfer, forming the more stable S_N2-f intermediate (INT). [d] Transition state cannot be located due to the instability of the associated product.

Supplementary Table S3. Energies relative to the separate reactants (in kcal mol^{-1}) of the stationary points (RC = reactant complex, TS = transition state, INT = intermediate, and P = product) of the S_N2-b and S_N2-f pathways.[a]

Nucleophile		Electrophile		
		CH_3OTf	CH_3CH_2OTf	$(CH_3)_2CHOTf$
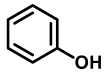	RC[b]	−1.9	−2.3	−2.6
	S_N2-b-TS	15.0	19.4	17.3
	S_N2-f-TS	49.3	35.1	22.7
	INT[c]	−1.1	−6.5	−4.3
	P	1.9	3.9	9.8
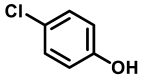	RC[b]	−2.1	−2.2	−2.5
	S_N2-b-TS	16.5	20.7	17.6
	S_N2-f-TS	50.0	35.2	22.7
	INT[c]	−7.0	−6.0	−4.4
	P	1.7	3.0	5.0
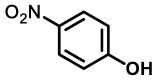	RC[b]	−2.5	−2.8	−3.0
	S_N2-b-TS	20.7	19.9	[d]
	S_N2-f-TS	50.1	35.0	22.6
	INT[c]	−5.1	−3.9	−1.2
	P	1.7	3.1	5.0
	RC[b]	−1.7	−1.8	−1.9
	S_N2-b-TS	9.0	14.0	15.7
	S_N2-f-TS	47.9	35.1	24.2
	INT[c]	−12.2	−11.1	−8.9
	P	0.4	1.2	4.5
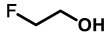	RC[b]	−2.0	−1.4	−2.2
	S_N2-b-TS	11.4	15.5	17.2
	S_N2-f-TS	47.9	34.6	24.0
	INT[c]	−10.1	−9.0	−7.6
	P	2.7	3.4	4.9
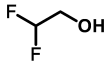	RC[b]	−2.2	−2.3	−2.3
	S_N2-b-TS	14.2	17.5	18.6
	S_N2-f-TS	49.3	35.3	24.4
	INT[c]	−8.6	−7.8	−6.4
	P	2.6	3.3	5.0
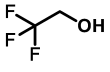	RC[b]	−1.8	−1.4	−1.3
	S_N2-b-TS	14.2	19.7	20.3
	S_N2-f-TS	49.9	35.5	24.3
	INT[c]	−8.0	−7.4	−6.1
	P	2.3	2.9	4.1
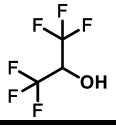	RC[b]	−2.7	−3.0	−2.8
	S_N2-b-TS	25.0	24.0	22.2
	S_N2-f-TS	50.0	33.9	21.8
	INT[c]	−4.7	−2.6	−1.6
	P	1.4	1.7	2.8

[a] Electronic energies computed at SMD(CH_2Cl_2)-(TightPNO)DLPNO-CCSD(T)/CBS(3,4/def2)//ZORA-OLYP/QZ4P. [b] Only the S_N2-f pathway involves a very weakly bound reactant complex RC, the energy of which is provided, while the S_N2-b pathway does not have a stable RC. [c] The product complex of the S_N2-b pathway results in charge separation, inducing a barrierless proton transfer, forming the more stable S_N2-f intermediate (INT). [d] Transition state cannot be located due to the instability of the associated product.

Supplementary Table S4. Energies relative to the separate reactants (in kcal mol^{-1}) of the stationary points (RC = reactant complex, TS = transition state, INT = intermediate, and P = product) of the S_N2-b and S_N2-f pathways.[a]

Nucleophile		Electrophile			
		CH_3OTf		CH_3CH_2OTf	
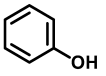	RC[b]	[d]	[d]	[d]	[d]
	S_N2-b-TS	28.6	(25.5)	28.8	(27.5)
	S_N2-f-TS	48.0	(48.8)	35.2	(36.6)
	INT[c]	−0.7	(−1.1)	0.4	[d]
	P	0.9	(1.1)	1.7	(3.3)
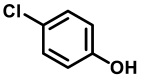	RC[b]	[d]	(−0.4)	[d]	(−0.3)
	S_N2-b-TS	29.4	(26.8)	29.4	(28.6)
	S_N2-f-TS	47.8	(48.6)	35.0	(36.4)
	INT[c]	−0.7	(−0.9)	0.6	0.6
	P	0.9	(0.9)	1.5	(1.8)
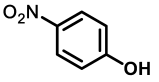	RC[b]	[d]	(−0.5)	[d]	(−0.5)
	S_N2-b-TS	32.8	(32.4)	32.7	(31.0)
	S_N2-f-TS	51.3	(52.0)	[e]	(38.3)
	INT[c]	[d]	[d]	[d]	[d]
	P	0.7	(0.7)	1.1	(1.6)
	RC[b]	[d]	[d]	[d]	[d]
	S_N2-b-TS	22.5	(19.2)	24.0	(22.7)
	S_N2-f-TS	48.5	(49.2)	35.9	(37.5)
	INT[c]	−5.9	(−5.6)	−4.9	(−4.0)
	P	−1.3	(−1.3)	1.2	(−0.5)
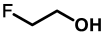	RC[b]	[d]	[d]	[d]	[d]
	S_N2-b-TS	24.3	(22.8)	25.5	(25.3)
	S_N2-f-TS	49.3	(50.0)	36.2	(37.7)
	INT[c]	−4.1	(−3.9)	−2.5	(−2.3)
	P	0.8	(1.0)	1.4	(1.6)
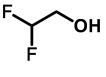	RC[b]	[d]	[d]	[d]	[d]
	S_N2-b-TS	26.6	(26.0)	27.3	(27.5)
	S_N2-f-TS	51.0	(51.5)	37.0	(38.7)
	INT[c]	−3.0	(−2.8)	−1.2	(−1.3)
	P	0.9	(1.0)	1.5	(1.5)
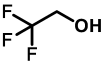	RC[b]	[d]	[d]	[d]	[d]
	S_N2-b-TS	28.2	(24.9)	28.5	(29.2)
	S_N2-f-TS	51.7	(52.4)	[e]	(39.0)
	INT[c]	[c]	(−2.5)	−1.0	(−1.0)
	P	0.8	(0.7)	1.3	(1.1)
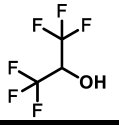	RC[b]	[d]	[d]	[d]	(−0.4)
	S_N2-b-TS	33.7	(35.8)	32.8	(34.0)
	S_N2-f-TS	53.8	(54.7)	[d]	(39.3)
	INT[c]	−0.9	(−0.7)	−1.0	[d]
	P	0.3	(0.4)	1.3	(0.5)

[a] Electronic energies computed at COSMO(CH_2Cl_2)-ZORA-OLYP/QZ4P with in brackets energies computed at COSMO(CH_2Cl_2)-ZORA-OLYP//ZORA-OLYP/QZ4P. [b] Only the S_N2-f pathway involves a very weakly bound reactant complex RC, the energy of which is provided, while the S_N2-b pathway does not have a stable RC. [c] The product complex of the S_N2-b pathway results in charge separation, inducing a barrierless proton transfer, forming the more stable S_N2-f intermediate (INT). [d] Stationary point is not stable. [e] Transition state cannot be located due to instability of the associated product.

Supplementary Table S5. Energies relative to the separate reactants (in kcal mol^{-1}) of the stationary points (RC = reactant complex, TS = transition state, INT = intermediate, and P = product) of the S_N2-b and S_N2-f pathways.[a]

Nucleophile		Electrophile		
		CH_3OTf	CH_3CH_2OTf	$(CH_3)_2CHOTf$
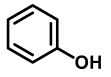	RC[b]	–3.0	–3.5	–3.0
	S_N2-b-TS	41.5	39.7	36.5
	S_N2-f-TS	48.3	39.4	29.3
	INT[c]	–4.4	–2.5	–1.2
	P	0.4	1.3	3.3
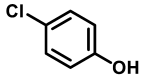	RC[b]	–3.3	–3.9	–3.5
	S_N2-b-TS	43.1	41.0	37.7
	S_N2-f-TS	48.1	39.1	29.5
	INT[c]	–4.1	–2.8	–1.0
	P	0.2	1.0	3.0
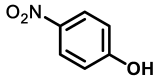	RC[b]	–3.9	–3.9	–4.0
	S_N2-b-TS	48.5	46.2	[d]
	S_N2-f-TS	51.0	41.0	30.2
	INT[c]	–2.9	–1.7	1.0
	P	0.0	0.6	2.4
	RC[b]	–2.2	–2.6	–2.7
	S_N2-b-TS	34.9	33.5	31.4
	S_N2-f-TS	49.6	41.1	32.0
	INT[c]	–8.1	–6.6	–4.1
	P	–2.4	–1.5	2.2
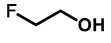	RC[b]	–2.0	–1.0	–1.8
	S_N2-b-TS	37.0	35.1	32.3
	S_N2-f-TS	50.3	41.7	31.6
	INT[c]	–6.3	–4.8	–2.7
	P	0.3	1.1	3.5
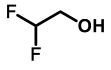	RC[b]	–2.3	–2.9	–2.1
	S_N2-b-TS	40.6	37.9	34.5
	S_N2-f-TS	51.9	42.4	32.2
	INT[c]	–5.1	–3.8	–2.2
	P	0.3	1.0	3.7
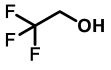	RC[b]	–2.9	–2.3	–2.3
	S_N2-b-TS	43.7	41.4	37.3
	S_N2-f-TS	52.5	42.5	31.6
	INT[c]	–4.9	–4.3	–2.8
	P	0.0	0.6	2.0
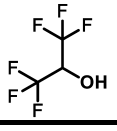	RC[b]	–3.4	–3.1	–3.5
	S_N2-b-TS	50.1	45.0	40.1
	S_N2-f-TS	54.5	43.3	31.9
	INT[c]	–3.2	–1.9	–0.6
	P	0.4	0.7	2.2

[a] Enthalpies computed at the ZORA-OLYP/QZ4P, relative to infinitely separated reactants. [b] Only the S_N2-f pathway involves a very weakly bound reactant complex RC, the energy of which is provided, while the S_N2-b pathway does not have a stable RC. [c] The product complex of the S_N2-b pathway results in charge separation, inducing a barrierless proton transfer, forming the more stable S_N2-f intermediate (INT). [d] Transition state cannot be located due to instability of the associated product.

Supplementary Table S6. Energies relative to the separate reactants (in kcal mol^{-1}) of the stationary points (RC = reactant complex, TS = transition state, INT = intermediate, and P = product) of the S_N2-b and S_N2-f pathways.[a]

Nucleophile		Electrophile		
		CH_3OTf	CH_3CH_2OTf	$(CH_3)_2CHOTf$
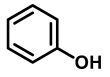	RC[b]	[d]	[d]	[d]
	S_N2-b-TS	56.7	50.1	48.3
	S_N2-f-TS	60.7	51.2	41.2
	INT[c]	[d]	[d]	[d]
	P	1.3	2.0	3.5
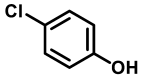	RC[b]	[d]	[d]	[d]
	S_N2-b-TS	58.6	53.5	49.6
	S_N2-f-TS	60.6	50.9	39.5
	INT[c]	[d]	[d]	[d]
	P	1.1	1.7	3.1
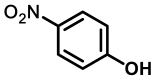	RC[b]	[d]	[d]	[d]
	S_N2-b-TS	63.7	59.0	[e]
	S_N2-f-TS	65.4	54.7	41.9
	INT[c]	[d]	[d]	[d]
	P	0.9	1.3	2.6
	RC[b]	[d]	[d]	[d]
	S_N2-b-TS	47.9	46.1	42.7
	S_N2-f-TS	61.4	52.5	43.2
	INT[c]	[d]	[d]	[d]
	P	–1.5	–0.8	2.2
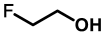	RC[b]	[d]	[d]	[d]
	S_N2-b-TS	50.3	47.8	43.7
	S_N2-f-TS	62.8	51.7	42.9
	INT[c]	[d]	[d]	[d]
	P	0.9	1.6	3.4
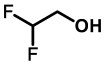	RC[b]	[d]	[d]	[d]
	S_N2-b-TS	54.3	51.0	46.2
	S_N2-f-TS	64.4	54.2	42.9
	INT[c]	[d]	[d]	[d]
	P	0.8	1.3	3.5
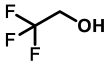	RC[b]	[d]	[d]	[d]
	S_N2-b-TS	57.5	54.3	49.0
	S_N2-f-TS	65.0	54.4	44.3
	INT[c]	[d]	[d]	[d]
	P	0.6	1.0	1.8
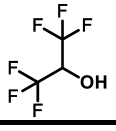	RC[b]	[d]	[d]	[d]
	S_N2-b-TS	63.9	58.4	52.2
	S_N2-f-TS	69.5	57.4	47.0
	INT[c]	[d]	[d]	[d]
	P	0.7	1.0	2.4

[a] Gibbs free energies computed at the ZORA-OLYP/QZ4P, relative to infinitely separated reactants. [b] Only the S_N2-f pathway involves a very weakly bound reactant complex RC, the energy of which is provided, while the S_N2-b pathway does not have a stable RC. [c] The product complex of the S_N2-b pathway results in charge separation, inducing a barrierless proton transfer, forming the more stable S_N2-f intermediate (INT). [d] Stationary point is not stable. [e] Transition state cannot be located due to instability of the associated product.

Supplementary Table S7. Energies relative to the separate reactants (in kcal mol^{-1}) of the stationary points (RC = reactant complex, TS = transition state, INT = intermediate, and P = product) of the S_N2-b and S_N2-f pathways.[a]

Nucleophile		Electrophile		
		CH_3OTf	CH_3CH_2OTf	$(CH_3)_2CHOTf$
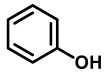	RC[b]	–0.5	–0.7	–0.6
	S_N2-b-TS	24.6	26.9	22.1
	S_N2-f-TS	46.4	34.2	20.6
	INT[c]	–1.2	[d]	[d]
	P	0.7	3.1	8.7
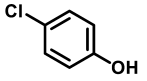	RC[b]	–1.0	–1.3	–0.8
	S_N2-b-TS	25.8	27.9	22.6
	S_N2-f-TS	46.0	33.9	20.9
	INT[c]	–1.0	[d]	[d]
	P	0.6	1.6	3.3
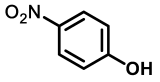	RC[b]	–1.1	–0.9	–1.0
	S_N2-b-TS	31.3	30.2	[e]
	S_N2-f-TS	48.8	35.1	20.4
	INT[c]	0.1	[d]	[d]
	P	0.3	1.4	2.9
	RC[b]	[d]	[d]	[d]
	S_N2-b-TS	19.1	22.3	20.6
	S_N2-f-TS	47.2	35.4	22.1
	INT[c]	–5.2	–3.5	–1.4
	P	–1.8	–0.9	2.2
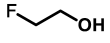	RC[b]	[d]	[d]	[d]
	S_N2-b-TS	22.6	24.9	22.4
	S_N2-f-TS	47.9	36.1	21.7
	INT[c]	–3.7	–1.9	-1.0
	P	0.4	1.2	3.3
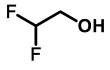	RC[b]	[d]	[d]	[d]
	S_N2-b-TS	25.8	27.0	23.9
	S_N2-f-TS	49.3	36.3	21.7
	INT[c]	–2.5	–0.8	–0.1
	P	0.4	1.1	2.5
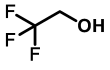	RC[b]	–0.6	[d]	[d]
	S_N2-b-TS	24.7	28.6	24.3
	S_N2-f-TS	50.1	36.5	21.1
	INT[c]	–2.1	–1.1	0.1
	P	0.2	0.8	1.7
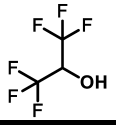	RC[b]	–1.4	–1.0	–1.7
	S_N2-b-TS	35.1	33.2	27.5
	S_N2-f-TS	51.6	35.9	21.9
	INT[c]	–0.9	[d]	[d]
	P	–0.2	0.2	1.4

[a] Enthalpies computed at the COSMO(CH_2Cl_2)-ZORA-OLYP/QZ4P, relative to infinitely separated reactants. [b] Only the S_N2-f pathway involves a very weakly bound reactant complex RC, the energy of which is provided, while the S_N2-b pathway does not have a stable RC. [c] The product complex of the S_N2-b pathway results in charge separation, inducing a barrierless proton transfer, forming the more stable S_N2-f intermediate (INT). [d] Stationary point is not stable. [e] Transition state cannot be located due to instability of the associated product.

Supplementary Table S8. Energies relative to the separate reactants (in kcal mol^{-1}) of the stationary points (RC = reactant complex, TS = transition state, INT = intermediate, and P = product) of the S_N2-b and S_N2-f pathways.[a]

Nucleophile		Electrophile		
		CH_3OTf	CH_3CH_2OTf	$(CH_3)_2CHOTf$
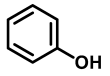	RC[b]	[d]	[d]	[d]
	S_N2-b-TS	36.3	33.7	30.4
	S_N2-f-TS	55.2	42.4	29.0
	INT[c]	[d]	[d]	[d]
	P	1.6	3.8	8.8
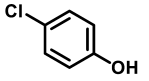	RC[b]	[d]	[d]	[d]
	S_N2-b-TS	37.8	36.9	31.0
	S_N2-f-TS	54.9	42.1	27.4
	INT[c]	[d]	[d]	[d]
	P	1.5	2.4	3.5
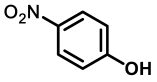	RC[b]	[d]	[d]	[d]
	S_N2-b-TS	42.9	39.5	[e]
	S_N2-f-TS	59.7	45.3	28.6
	INT[c]	[d]	[d]	[d]
	P	1.2	2.2	3.1
	RC[b]	[d]	[d]	[d]
	S_N2-b-TS	28.5	31.3	28.3
	S_N2-f-TS	55.6	43.3	29.7
	INT[c]	[d]	[d]	[d]
	P	–1.0	–0.2	2.1
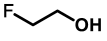	RC[b]	[d]	[d]	[d]
	S_N2-b-TS	32.3	34.1	30.3
	S_N2-f-TS	56.8	42.6	29.5
	INT[c]	[d]	[d]	[d]
	P	1.0	1.6	3.1
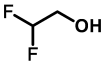	RC[b]	[d]	[d]	[d]
	S_N2-b-TS	35.9	36.5	32.1
	S_N2-f-TS	58.3	44.6	28.9
	INT[c]	[d]	[d]	[d]
	P	1.0	1.4	2.3
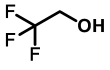	RC[b]	[d]	[d]	[d]
	S_N2-b-TS	35.0	38.0	32.5
	S_N2-f-TS	59.1	44.8	30.3
	INT[c]	[d]	[d]	[d]
	P	0.8	1.1	1.6
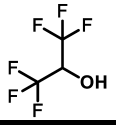	RC[b]	[d]	[d]	[d]
	S_N2-b-TS	45.4	43.1	36.0
	S_N2-f-TS	63.0	46.5	33.5
	INT[c]	[d]	[d]	[d]
	P	0.1	0.5	1.6

[a] Gibbs free energies (TS were corrected by the Martin-Hay-Pratt approach) computed at the COSMO(CH_2Cl_2)-ZORA-OLYP/QZ4P, relative to infinitely separated reactants. [b] Only the S_N2-f pathway involves a very weakly bound reactant complex RC, the energy of which is provided, while the S_N2-b pathway does not have a stable RC. [c] The product complex of the S_N2-b pathway results in charge separation, inducing a barrierless proton transfer, forming the more stable S_N2-f intermediate (INT). [d] Stationary point is not stable. [e] Transition state cannot be located due to instability of the associated product.

Supplementary Table S9. Heterolytic proton affinity (ΔH_{PA}) energies in in kcal mol^{-1}.[a–d]

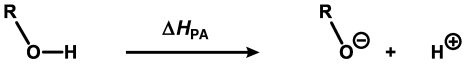

Alcohol	OLYP[a]	(CH_2Cl_2)-OLYP[b]	DLPNO-CCSD(T)[c]	(CH_2Cl_2)-DLPNO-CCSD(T)[d]
Phenol	348.4	297.9	349.0	304.0
p-Chlorophenol	341.9	296.1	342.4	301.8
p-Nitrophenol	324.7	285.8	327.6	293.8
Ethanol	375.0	315.1	379.0	325.5
2-Fluoroethanol	369.8	311.7	373.7	322.4
2,2-Difluoroethanol	364.2	308.0	366.3	318.0
2,2,2-Trifluoroethanol	359.7	305.3	361.4	314.6
1,1,1,3,3,3-Hexafluoro-2-propanol	343.6	295.9	345.1	303.3

[a] Computed at ZORA-OLYP/QZ4P. [b] Computed at COSMO(CH_2Cl_2)-ZORA-OLYP/QZ4P// ZORA-OLYP/QZ4P. [c] Computed at (TightPNO)DLPNO-CCSD(T)/CBS(3,4/def2)//ZORA-OLYP/QZ4P. [d] Computed at SMD(CH_2Cl_2)-(TightPNO)DLPNO-CCSD(T)/CBS(3,4/def2)//ZORA-OLYP/QZ4P.

Supplementary Table S10. HOMO energies of nucleophiles.[a,b]

	HOMO energy (eV)	
Alcohol	OLYP[a]	(CH_2Cl_2)-OLYP[b]
Phenol	–5.374	–5.459
p-Chlorophenol	–5.395	–5.376
p-Nitrophenol	–6.269	–6.049
Ethanol	–6.112	–6.249
2-Fluoroethanol	–6.473	–6.520
2,2-Difluoroethanol	–6.829	–6.757
2,2,2-Trifluoroethanol	–7.132	–7.016
1,1,1,3,3,3-Hexafluoro-2-propanol	–7.727	–7.547

[a] Computed at ZORA-OLYP/QZ4P. [b] Computed at COSMO(CH_2Cl_2)-ZORA-OLYP/QZ4P// ZORA-OLYP/QZ4P.

Supplementary Table S11. LUMO energies of nucleophiles.[a,b]

	LUMO energy (eV)	
Alcohol	OLYP[a]	(CH_2Cl_2)-OLYP[b]
Phenol	–1.052	–1.100
p-Chlorophenol	–1.409	–1.324
p-Nitrophenol	–3.108	–3.216
Ethanol	–0.845	–0.650
2-Fluoroethanol	–0.776	–0.640
2,2-Difluoroethanol	–0.902	–0.644
2,2,2-Trifluoroethanol	–1.088	–0.753
1,1,1,3,3,3-Hexafluoro-2-propanol	–1.106	–0.788

[a] Computed at ZORA-OLYP/QZ4P. [b] Computed at COSMO(CH_2Cl_2)-ZORA-OLYP/QZ4P// ZORA-OLYP/QZ4P.

Supplementary Table S12. Voronoi deformation density on the oxygen and hydrogen atom of the alcohol group of nucleophiles.

	Voronoi deformation density (VDD)			
	OLYP[a]		(CH_2Cl_2)-OLYP[b]	
Alcohol	O-atom	H-atom	O-atom	H-atom
Phenol	–0.181	0.196	–0.205	0.222
p-Chlorophenol	–0.177	0.200	–0.200	0.225
p-Nitrophenol	–0.163	0.209	–0.178	0.237
Ethanol	–0.225	0.156	–0.262	0.177
2-Fluoroethanol	–0.229	0.168	–0.262	0.181
2,2-Difluoroethanol	–0.220	0.170	–0.247	0.187
2,2,2-Trifluoroethanol	–0.213	0.173	–0.242	0.192
1,1,1,3,3,3-Hexafluoro-2-propanol	–0.201	0.183	–0.220	0.200

[a] Computed at ZORA-OLYP/QZ4P. [b] Computed at COSMO(CH_2Cl_2)-ZORA-OLYP/QZ4P// ZORA-OLYP/QZ4P.

Supplementary Table S13. R_3C–OTf (R = H or Me) bond lengths (in Å) and heterolytic bond dissociation energies $\Delta H_{BDE,hetero}$ energies.

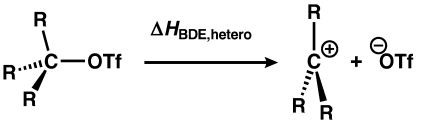

Electrophile	*r* (C–X)[a]	OLYP[a]	(CH_2Cl_2)-OLYP[b]	DLPNO-CCSD(T) [c]	CH_2Cl_2-DLPNO-CCSD(T) [d]
CH_3OTf	1.457	190.4	68.3	189.3	73.5
CH_3CH_2OTf	1.475	146.8	37.5	152.6	44.8
$(CH_3)_2CH_2OTf$	1.496	125.9	23.6	139.8	38.3

[a] Computed at ZORA-OLYP/QZ4P.[b] Computed at COSMO(CH_2Cl_2)-ZORA-OLYP/QZ4P// ZORA-OLYP/QZ4P. [c] Computed at (TightPNO)DLPNO-CCSD(T)/CBS(3,4/def2)//ZORA-OLYP/QZ4P. [d] Computed at SMD(CH_2Cl_2)-(TightPNO)DLPNO-CCSD(T)/CBS(3,4/def2)//ZORA-OLYP/QZ4P.

References

(1) Hughes, E. D.; Ingold, C. K.; Patel, C. S. 135. Influence of Poles and Polar Linkings on the Course Pursued by Elimination Reactions. Part XVI. Mechanism of the Thermal Decomposition of Quaternary Ammonium Compounds. *J. Chem. Soc.* **1933**, 526–530.

(2) Hughes, E. D.; Ingold, C. K. 55. Mechanism of Substitution at a Saturated Carbon Atom. Part IV. A Discussion of Constitutional and Solvent Effects on the Mechanism, Kinetics, Velocity, and Orientation of Substitution. *J. Chem. Soc.* **1935**, 244–255.

(3) Hughes, E. D.; Juliusburger, F.; Masterman, S.; Topley, B.; Weiss, J. 362. Aliphatic Substitution and the Walden Inversion. Part I. *J. Chem. Soc.* **1935**, 1525–1529.

(4) Ingold, S. C. *Structure and Mechanism in Organic Chemistry*, 2nd ed.; Cornell University Press: Ithaca, 1969.

(5) Cowdrey, W. A.; Hughes, E. D.; Ingold, C. K.; Masterman, S.; Scott, A. D. 257. Reaction Kinetics and the Walden Inversion. Part VI. Relation of Steric Orientation to Mechanism in Substitutions Involving Halogen Atoms and Simple or Substituted Hydroxyl Groups. *J. Chem. Soc.* **1937**, 1252–1271.

(6) Glukhovtsev, M. N.; Pross, A.; Schlegel, H. B.; Bach, R. D.; Radom, L. Gas-Phase Identity S_N2 Reactions of Halide Anions and Methyl Halides with Retention of Configuration. *J. Am. Chem. Soc.* **1996**, *118* (45), 11258–11264.

(7) Uggerud, E. Reactivity Trends and Stereospecificity in Nucleophilic Substitution Reactions. *J. Phys. Org. Chem.* **2006**, *19* (8–9), 461–466.

(8) Bogdanov, B.; McMahon, T. B. Thermochemistry and Structures of Solvated S_N2 Complexes and Transition States in the Gas Phase: Experiment and Theory. *Int. J. Mass Spectrom.* **2005**, *241* (2), 205–223.

(9) Wester, R. Fifty Years of Nucleophilic Substitution in the Gas Phase. *Mass Spectrom. Rev.* **2022**, *41* (4), 627–644.

(10) Barlow, S. E.; Van Doren, J. M.; Bierbaum, V. M. The Gas Phase Displacement Reaction of Chloride Ion with Methyl Chloride as a Function of Kinetic Energy. *J. Am. Chem. Soc.* **1988**, *110* (21), 7240–7242.

(11) Angel, L. A.; Ervin, K. M. Dynamics of the Gas-Phase Reactions of Fluoride Ions with Chloromethane. *J. Phys. Chem. A* **2001**, *105* (16), 4042–4051.

(12) Mensa-Bonsu, G.; Tozer, D. J.; Verlet, J. R. R. Photoelectron Spectroscopic Study of $I^-{\cdot}ICF_3$: A Frontside Attack S_N2 Pre-Reaction Complex. *Phys. Chem. Chem. Phys.* **2019**, *21* (26), 13977–13985.

(13) Li, G.; Hase, W. L. Ab Initio Direct Dynamics Trajectory Study of the $Cl^- + CH_3Cl$ S_N2 Reaction at High Reagent Translational Energy. *J. Am. Chem. Soc.* **1999**, *121* (30), 7124–7129.

(14) Bento, A. P.; Bickelhaupt, F. M. Nucleophilicity and Leaving-Group Ability in Frontside and Backside S_N2 Reactions. *J. Org. Chem.* **2008**, *73* (18), 7290–7299.

(15) Bento, A. P.; Bickelhaupt, F. M. Frontside versus Backside S_N2 Substitution at Group 14 Atoms: Origin of Reaction Barriers and Reasons for Their Absence. *Chem. – Asian J.* **2008**, *3* (10), 1783–1792.

(16) Glukhovtsev, M. N.; Pross, A.; Radom, L. Gas-Phase Non-Identity S_N2 Reactions of Halide Anions with Methyl Halides: A High-Level Computational Study. *J. Am. Chem. Soc.* **1996**, *118* (26), 6273–6284.

(17) Savoo, N.; Laloo, J. Z. A.; Rhyman, L.; Ramasami, P.; Bickelhaupt, F. M.; Poater, J. Activation Strain Analyses of Counterion and Solvent Effects on the Ion-Pair S_N2 Reaction of NH_2^- and CH_3Cl. *J. Comput. Chem.* **2020**, *41* (4), 317–327.

(18) Deng, L.; Branchadell, V.; Ziegler, T. Potential Energy Surfaces of the Gas-Phase S_N2 Reactions $X^- + CH_3X = XCH_3 + X^-$ (X = F, Cl, Br, I): A Comparative Study by Density Functional Theory and Ab Initio Methods. *J. Am. Chem. Soc.* **1994**, *116* (23), 10645–10656.

(19) Papp, P.; Tajti, V.; Czakó, G. Numerical Separation of the Front-Side Attack and Double-Inversion Retention Pathways of S_N2 Reactions. *Chem. Phys. Lett.* **2020**, *755*, 137780.

(20) Yang, Z.-Z.; Ding, Y.-L.; Zhao, D.-X. Theoretical Analysis of Gas-Phase Front-Side Attack Identity S_N2(C) and S_N2(Si) Reactions with Retention of Configuration. *J. Phys. Chem. A* **2009**, *113* (18), 5432–5445.

(21) Szabó, I.; Czakó, G. Revealing a Double-Inversion Mechanism for the $F^- + CH_3Cl$ S_N2 Reaction. *Nat. Commun.* **2015**, *6* (1), 5972.

(22) Tasi, D. A.; Fábián, Z.; Czakó, G. Rethinking the $X^- + CH_3Y$ [X = OH, SH, CN, NH_2, PH_2; Y = F, Cl, Br, I] S_N2 Reactions. *Phys. Chem. Chem. Phys.* **2019**, *21* (15), 7924–7931.

(23) Tasi, D. A.; Fábián, Z.; Czakó, G. Benchmark Ab Initio Characterization of the Inversion and Retention Pathways of the $OH^- + CH_3Y$ [Y = F, Cl, Br, I] S_N2 Reactions. *J. Phys. Chem. A* **2018**, *122* (26), 5773–5780.

(24) Tasi, D. A.; Czakó, G. Unconventional S_N2 Retention Pathways Induced by Complex Formation: High-Level Dynamics Investigation of the $NH_2^- + CH_3I$ Polyatomic Reaction. *J. Chem. Phys.* **2022**, *156* (18), 184306.

(25) Okamoto, K.; Kinoshita, T.; Oshida, T.; Yamamoto, T.; Ito, Y.; Dohi, M. Retentive Solvolysis. Part XI. Retentive Phenolyses of Optically Active Secondary and Tertiary Systems without a Group Imposing Configurational Restriction. *J. Chem. Soc. Perkin Trans. 2* **1976**, 1617–1627.

(26) Okamoto, K.; Kinoshita, T.; Shingu, H. The Retentive Solvolysis. VII. Structural Effect of the Leaving Group on the Steric Course of the S_N1 Phenolysis of 1-Phenylethyl Systems. *Bull. Chem. Soc. Jpn.* **1970**, *43* (5), 1545–1553.

(27) Kinoshita, T.; Ueno, T.; Ikai, K.; Fujiwara, M.; Okamoto, K. Retentive Solvolysis. 16. Reinvestigation of the Retentive Phenolysis of 1-Phenylethyl Chloride. The Mechanism and the Structure of Ion Pair Intermediate. *Bull. Chem. Soc. Jpn.* **1988**, *61* (9), 3273–3282.

(28) Okamoto, K.; Kinoshita, T.; Osada, Y. Phenolysis and Competing Methanolysis of Optically Active 1-Phenylethyl Chloride in Sterically Hindered 2,6-Dialkylphenol Solvents. *J. Chem. Soc. Perkin Trans. 2* **1975**, 253–257.

(29) Okamoto, K. Solvent Molecules and Carbocation Intermediates in Solvolyses. *Pure Appl. Chem.* **1984**, *56* (12), 1797–1808.

(30) Dauner, H.; Lenoir, D.; Ugi, I. Der Retentive Verlauf Nukleophiler Substitutionen an 7-*Exo*-Norcaryltriflat. *Z. Für Naturforschung B* **1979**, *34* (12), 1745–1749.

(31) Stohrer, W.-D.; Schmieder, K. R. Ein MO-Modell für die S_N2-Reaktion mit Retention. *Chem. Ber.* **1976**, *109* (1), 285–305.

(32) Ruggiero, G. D.; Williams, I. H. Kinetic Isotope Effects for Gas Phase S_N2 Methyl Transfer: A Computational Study of Anionic and Cationic Identity Reactions. *J. Chem. Soc. Perkin Trans. 2* **2002**, 591–597.

(33) Kubota, Y.; Kunikata, M.; Haraguchi, K.; Tanaka, H. Solvent Effect Observed in Nucleophilic Substitution of 4′-(Benzoyloxy)Cordycepin with $AlMe_3$: Stereochemical Evidence for S_Ni Mechanism. *J. Org. Chem.* **2009**, *74* (9), 3402–3405.

(34) Nishi, N.; Sueoka, K.; Iijima, K.; Sawa, R.; Takahashi, D.; Toshima, K. Stereospecific β-l-Rhamnopyranosylation through an S_Ni-Type Mechanism by Using Organoboron Reagents. *Angew. Chem. Int. Ed.* **2018**, *57* (42), 13858–13862.

(35) Fu, Y.; Bernasconi, L.; Liu, P. Ab Initio Molecular Dynamics Simulations of the S_N1/S_N2 Mechanistic Continuum in Glycosylation Reactions. *J. Am. Chem. Soc.* **2021**, *143* (3), 1577–1589.

(36) Gómez, H.; Polyak, I.; Thiel, W.; Lluch, J. M.; Masgrau, L. Retaining Glycosyltransferase Mechanism Studied by QM/MM Methods: Lipopolysaccharyl-α-1,4-Galactosyltransferase C Transfers α-Galactose via an Oxocarbenium Ion-like Transition State. *J. Am. Chem. Soc.* **2012**, *134* (10), 4743–4752.

(37) Persson, K.; Ly, H. D.; Dieckelmann, M.; Wakarchuk, W. W.; Withers, S. G.; Strynadka, N. C. J. Crystal Structure of the Retaining Galactosyltransferase LgtC from *Neisseria Meningitidis* in Complex with Donor and Acceptor Sugar Analogs. *Nat. Struct. Biol.* **2001**, *8* (2), 166–175.

(38) Gibson, R. P.; Turkenburg, J. P.; Charnock, S. J.; Lloyd, R.; Davies, G. J. Insights into Trehalose Synthesis Provided by the Structure of the Retaining Glucosyltransferase OtsA. *Chem. Biol.* **2002**, *9* (12), 1337–1346.

(39) Vetting, M. W.; Frantom, P. A.; Blanchard, J. S. Structural and Enzymatic Analysis of MshA from *Corynebacterium Glutamicum*. *J. Biol. Chem.* **2008**, *283* (23), 15834–15844.

(40) Lee, S. S.; Hong, S. Y.; Errey, J. C.; Izumi, A.; Davies, G. J.; Davis, B. G. Mechanistic Evidence for a Front-Side, S_Ni-Type Reaction in a Retaining Glycosyltransferase. *Nat. Chem. Biol.* **2011**, *7* (9), 631–638.

(41) Iglesias-Fernández, J.; Hancock, S. M.; Lee, S. S.; Khan, M.; Kirkpatrick, J.; Oldham, N. J.; McAuley, K.; Fordham-Skelton, A.; Rovira, C.; Davis, B. G. A Front-Face "S_Ni Synthase" Engineered from a Retaining "Double-S_N2" Hydrolase. *Nat. Chem. Biol.* **2017**, *13* (8), 874–881.

(42) Sinnott, M. L.; Jencks, W. P. Solvolysis of D-Glucopyranosyl Derivatives in Mixtures of Ethanol and 2,2,2-Trifluoroethanol. *J. Am. Chem. Soc.* **1980**, *102* (6), 2026–2032.

(43) $(CH_3)_3COTf$ as electrophile was excluded because it is less likely that this electrophile undergoes S_N2-like reactions, but instead proceeds through a more dissociated mechanism. It was attempted to identify the transition states, however, no S_N2 transition states could be located.

(44) Vorm, S. van der; Hansen, T.; S. Overkleeft, H.; Marel, G. A. van der; C. Codée, J. D. The Influence of Acceptor Nucleophilicity on the Glycosylation Reaction Mechanism. *Chem. Sci.* **2017**, *8* (3), 1867–1875.

(45) Vorm, S. van der; Hansen, T.; Hengst, J. M. A. van; Overkleeft, H. S.; Marel, G. A. van der; Codée, J. D. C. Acceptor Reactivity in Glycosylation Reactions. *Chem. Soc. Rev.* **2019**, *48* (17), 4688–4706.

(46) Vermeeren, P.; van der Lubbe, S. C. C.; Fonseca Guerra, C.; Bickelhaupt, F. M.; Hamlin, T. A. Understanding Chemical Reactivity Using the Activation Strain Model. *Nat. Protoc.* **2020**, *15* (2), 649–667.

(47) Bickelhaupt, F. M.; Houk, K. N. Analyzing Reaction Rates with the Distortion/Interaction-Activation Strain Model. *Angew. Chem. Int. Ed.* **2017**, *56* (34), 10070–10086.

(48) Vermeeren, P.; Hamlin, T. A.; Bickelhaupt, F. M. Chemical Reactivity from an Activation Strain Perspective. *Chem. Commun.* **2021**, *57* (48), 5880–5896.

(49) Hamlin, T. A.; Vermeeren, P.; Guerra, C. F.; Bickelhaupt, F. M. Energy Decomposition Analysis in the Context of Quantitative Molecular Orbital Theory. In *Complementary Bonding Analysis*; De Gruyter, 2021; pp 199–212.

(50) Bickelhaupt, F. M.; Baerends, E. J. Kohn-Sham Density Functional Theory: Predicting and Understanding Chemistry. In *Reviews in Computational Chemistry*; John Wiley & Sons, Ltd: New York, 2000; pp 1–86.

(51) van Meer, R.; Gritsenko, O. V.; Baerends, E. J. Physical Meaning of Virtual Kohn–Sham Orbitals and Orbital Energies: An Ideal Basis for the Description of Molecular Excitations. *J. Chem. Theory Comput.* **2014**, *10* (10), 4432–4441.

(52) The S_N2-b and S_N2-f triflate inversions ($CH_3OTf/CH_3CH_2OTf/(CH_3)_2CHOTf + TfO^-$) were computed and can be found in Table S1. The ASM and EDA diagrams can be found in Figure S1.

(53) Hamlin, T. A.; Swart, M.; Bickelhaupt, F. M. Nucleophilic Substitution (S_N2): Dependence on Nucleophile, Leaving Group, Central Atom, Substituents, and Solvent. *ChemPhysChem* **2018**, *19* (11), 1315–1330.

(54) Bickelhaupt, F. M. Base-Induced 1,4-Elimination:Insights from Theory and Mass Spectrometry. *Mass Spectrom. Rev.* **2001**, *20* (6), 347–361.

(55) For reactions in the condensed phase, the activation barrier is computed as the difference in energy between the transition state and the reactant complex (in case the RC is not stable, it is relative to the separate reactants). Note, in solution the RCs are not stable and thus not relevant.

(56) Weigend, F.; Ahlrichs, R. Balanced Basis Sets of Split Valence, Triple Zeta Valence and Quadruple Zeta Valence Quality for H to Rn: Design and Assessment of Accuracy. *Phys. Chem. Chem. Phys.* **2005**, *7* (18), 3297–3305.

(57) Weigend, F. Accurate Coulomb-Fitting Basis Sets for H to Rn. *Phys. Chem. Chem. Phys.* **2006**, *8* (9), 1057–1065.

(58) Hellweg, A.; Hättig, C.; Höfener, S.; Klopper, W. Optimized Accurate Auxiliary Basis Sets for RI-MP2 and RI-CC2 Calculations for the Atoms Rb to Rn. *Theor. Chem. Acc.* **2007**, *117* (4), 587–597.

(59) Weigend, F. Hartree–Fock Exchange Fitting Basis Sets for H to Rn. *J. Comput. Chem.* **2008**, *29* (2), 167–175.

(60) Riplinger, C.; Sandhoefer, B.; Hansen, A.; Neese, F. Natural Triple Excitations in Local Coupled Cluster Calculations with Pair Natural Orbitals. *J. Chem. Phys.* **2013**, *139* (13), 134101.

(61) Liakos, D. G.; Sparta, M.; Kesharwani, M. K.; Martin, J. M. L.; Neese, F. Exploring the Accuracy Limits of Local Pair Natural Orbital Coupled-Cluster Theory. *J. Chem. Theory Comput.* **2015**, *11* (4), 1525–1539.

(62) Guo, Y.; Riplinger, C.; Becker, U.; Liakos, D. G.; Minenkov, Y.; Cavallo, L.; Neese, F. Communication: An Improved Linear Scaling Perturbative Triples Correction for the Domain Based Local Pair-Natural Orbital Based Singles and Doubles Coupled Cluster Method [DLPNO-CCSD(T)]. *J. Chem. Phys.* **2018**, *148* (1), 011101.

(63) Neese, F. The ORCA Program System. *WIREs Comput. Mol. Sci.* **2012**, *2* (1), 73–78.

(64) Neese, F. Software Update: The ORCA Program System—Version 5.0. *WIREs Comput. Mol. Sci.* **2022**, *12* (5), e1606.

(65) Legault, C. Y. CYLview, 2009. http://www.cylview.org.

(66) Vermeeren, P.; Hansen, T.; Jansen, P.; Swart, M.; Hamlin, T. A.; Bickelhaupt, F. M. A Unified Framework for Understanding Nucleophilicity and Protophilicity in the S_N2/E2 Competition. *Chem. – Eur. J.* **2020**, *26* (67), 15538–15548.

(67) Vermeeren, P.; Hansen, T.; Grasser, M.; Silva, D. R.; Hamlin, T. A.; Bickelhaupt, F. M. S_N2 versus E2 Competition of F^- and PH_2^- Revisited. *J. Org. Chem.* **2020**, *85* (21), 14087–14093.

(68) Hansen, T.; Roozee, J. C.; Bickelhaupt, F. M.; Hamlin, T. A. How Solvation Influences the S_N2 versus E2 Competition. *J. Org. Chem.* **2022**, *87* (3), 1805–1813.

(69) Hansen, T.; Vermeeren, P.; de Jong, L.; Bickelhaupt, F. M.; Hamlin, T. A. S_N2 versus S_N2' Competition. *J. Org. Chem.* **2022**, *87* (14), 8892–8901.

(70) Wu, X.-P.; Sun, X.-M.; Wei, X.-G.; Ren, Y.; Wong, N.-B.; Li, W.-K. Exploring the Reactivity Trends in the E2 and S_N2 Reactions of $X^- + CH_3CH_2Cl$ (X = F, Cl, Br, HO, HS, HSe, NH_2 PH_2, AsH_2, CH_3, SiH_3, and GeH_3). *J. Chem. Theory Comput.* **2009**, *5* (6), 1597–1606.

(71) Hansen, T.; Vermeeren, P.; Zijderveld, K. W. J.; Bickelhaupt, F. M.; Hamlin, T. A. S_N2 versus E2 Competition of Cyclic Ethers. *Chem. – Eur. J.* **2023**, *29* (50), e202301308.

(72) Borges dos Santos, R. M.; Martinho Simões, J. A. Energetics of the O–H Bond in Phenol and Substituted Phenols: A Critical Evaluation of Literature Data. *J. Phys. Chem. Ref. Data* **1998**, *27* (3), 707–739.

(73) Wright, J. S.; Carpenter, D. J.; McKay, D. J.; Ingold, K. U. Theoretical Calculation of Substituent Effects on the O−H Bond Strength of Phenolic Antioxidants Related to Vitamin E. *J. Am. Chem. Soc.* **1997**, *119* (18), 4245–4252.

(74) Lide, D. R. *CRC Hand Book of Chemistry and Physics*, 78th ed.; CRC Press: New York, 1997.

(75) Taft, R. W.; Koppel, I. A.; Topsom, R. D.; Anvia, F. Acidities of OH Compounds, Including Alcohols, Phenol, Carboxylic Acids, and Mineral Acids. *J. Am. Chem. Soc.* **1990**, *112* (6), 2047–2052.

(76) Bartmess, J. E.; Scott, J. A.; McIver, R. T. Scale of Acidities in the Gas Phase from Methanol to Phenol. *J. Am. Chem. Soc.* **1979**, *101* (20), 6046–6056.

(77) Graul, S. T.; Schnute, M. E.; Squires, R. R. Gas-Phase Acidities of Carboxylic Acids and Alcohols from Collision-Induced Dissociation of Dimer Cluster Ions. *Int. J. Mass Spectrom. Ion Process.* **1990**, *96* (2), 181–198.

(78) Ramond, T. M.; Davico, G. E.; Schwartz, R. L.; Lineberger, W. C. Vibronic Structure of Alkoxy Radicals via Photoelectron Spectroscopy. *J. Chem. Phys.* **2000**, *112* (3), 1158–1169.
(79) Chandra, A. K.; Uchimaru, T. The O-H Bond Dissociation Energies of Substituted Phenols and Proton Affinities of Substituted Phenoxide Ions: A DFT Study. *Int. J. Mol. Sci.* **2002**, *3* (4), 407–422.
(80) Uggerud, E.; Bache-Andreassen, L. Theoretical Models and Experimental Data for Reactions between Water and Protonated Alcohols: Substitution and Elimination Mechanisms. *Chem. – Eur. J.* **1999**, *5* (6), 1917–1930.
(81) Laerdahl, J. K.; Uggerud, E. Nucleophilic Identity Substitution Reactions. The Reaction between Water and Protonated Alcohols. *Org. Biomol. Chem.* **2003**, *1* (16), 2935–2942.
(82) Laerdahl, J. K.; Bache-Andreassen, L.; Uggerud, E. Nucleophilic Identity Substitution Reactions. The Reaction between Ammonia and Protonated Amines. *Org. Biomol. Chem.* **2003**, *1* (16), 2943–2950.
(83) K. Laerdahl, J.; U. Civcir, P.; Bache-Andreassen, L.; Uggerud, E. Nucleophilic Identity Substitution Reactions. The Reaction between Hydrogen Fluoride and Protonated Alkyl Fluorides. *Org. Biomol. Chem.* **2006**, *4* (1), 135–141.
(84) To assess the accuracy of a single point analysis with COSMO, the geometries of the reaction profiles were recomputed using COSMO of a selection of the systems, which showed similar reaction trends (Supplementary Table S4 and S15).
(85) Dichloromethane (nonpolar aprotic solvent; ε = 9) was selected as solvent.
(86) Ji, X.; Zhao, C.; Xie, J. Investigating the Role of Halogen-Bonded Complexes in Microsolvated $Y^-(H2O)_n$ + CH_3I S_N2 Reactions. *Phys. Chem. Chem. Phys.* **2021**, *23* (11), 6349–6360.
(87) Importantly, the computed trends in reactivity at COSMO(CH_2Cl_2)ZORA-OLYP/QZ4P agree well with those calculated at the more accurate SMD(CH_2Cl_2)-(TightPNO)DLPNO-CCSD(T)/CBS(3,4/def2)//ZORA-OLYP/QZ4 level (see Table S3).
(88) Svatunek, D.; Hansen, T.; Houk, K. N.; Hamlin, T. A. How the Lewis Base F^- Catalyzes the 1,3-Dipolar Cycloaddition between Carbon Dioxide and Nitrilimines. *J. Org. Chem.* **2021**, *86* (5), 4320–4325.
(89) van der Ham, A.; Hansen, T.; Lodder, G.; Codée, J. D. C.; Hamlin, T. A.; Filippov, D. V. Computational and NMR Studies on the Complexation of Lithium Ion to 8-Crown-4. *ChemPhysChem* **2019**, *20* (16), 2103–2109.
(90) Hansen, T.; Sun, X.; Dalla Tiezza, M.; van Zeist, W.-J.; Poater, J.; Hamlin, T. A.; Bickelhaupt, F. M. C(sp^n)–X (N=1–3) Bond Activation by Palladium. *Chem. – Eur. J.* **2022**, *28* (26), e202103953.
(91) Hansen, T.; Vermeeren, P.; Bickelhaupt, F. M.; Hamlin, T. A. Stability of Alkyl Carbocations. *Chem. Commun.* **2022**, *58* (86), 12050–12053.
(92) Hansen, T.; Nin-Hill, A.; Codée, J. D. C.; Hamlin, T. A.; Rovira, C. Rational Tuning of the Reactivity of Three-Membered Heterocycle Ring Openings via S_N2 Reactions. *Chem. – Eur. J.* **2022**, *28* (60), e202201649.
(93) Hansen, T.; Vermeeren, P.; Bickelhaupt, F. M.; Hamlin, T. A. Origin of the α-Effect in S_N2 Reactions. *Angew. Chem. Int. Ed.* **2021**, *60* (38), 20840–20848.
(94) Vermeeren, P.; van Zeist, W.-J.; Hamlin, T. A.; Fonseca Guerra, C.; Bickelhaupt, F. M. Not Carbon s–p Hybridization, but Coordination Number Determines C–H and C–C Bond Length. *Chem. – Eur. J.* **2021**, *27* (24), 7074–7079.
(95) Hansen, T.; Vermeeren, P.; Haim, A.; van Dorp, M. J. H.; Codée, J. D. C.; Bickelhaupt, F. M.; Hamlin, T. A. Regioselectivity of Epoxide Ring-Openings via S_N2 Reactions Under Basic and Acidic Conditions. *Eur. J. Org. Chem.* **2020**, *2020* (25), 3822–3828.
(96) For strong anionic nucleophiles, shifting towards an interaction-controlled regime, one can expect an increase in activation energies for more substituted electrophiles as a result of the abovementioned weakening of the nucleophile–electrophile interactions due to the increased steric demand of these systems.
(97) Herschlag, D.; Pinney, M. M. Hydrogen Bonds: Simple after All? *Biochemistry* **2018**, *57* (24), 3338–3352.
(98) van der Lubbe, S. C. C.; Zaccaria, F.; Sun, X.; Fonseca Guerra, C. Secondary Electrostatic Interaction Model Revised: Prediction Comes Mainly from Measuring Charge Accumulation in Hydrogen-Bonded Monomers. *J. Am. Chem. Soc.* **2019**, *141* (12), 4878–4885.
(99) When anionic TfO^- is used as nucleophile in the herein studied reaction system a similar behavior as Bickelhaupt and co-workers reported is found (see Figure S1 and Table S1).
(100) Note that steric repulsion between the reactants can manifest in both: (i) the strain energy, because steric repulsion deforms the fragments (*i.e.*, reactants), and (ii) the steric (Pauli) repulsion found in the nucleophile–electrophile interaction.
(101) Fonseca Guerra, C.; Handgraaf, J.-W.; Baerends, E. J.; Bickelhaupt, F. M. Voronoi Deformation Density (VDD) Charges: Assessment of the Mulliken, Bader, Hirshfeld, Weinhold, and VDD Methods for Charge Analysis. *J. Comput. Chem.* **2004**, *25* (2), 189–210.
(102) Velde, G. te; Bickelhaupt, F. M.; Baerends, E. J.; Guerra, C. F.; Gisbergen, S. J. A. van; Snijders, J. G.; Ziegler, T. Chemistry with ADF. *J. Comput. Chem.* **2001**, *22* (9), 931–967.
(103) Fonseca Guerra, C.; Snijders, J. G.; te Velde, G.; Baerends, E. J. Towards an Order-N DFT Method. *Theor. Chem. Acc.* **1998**, *99* (6), 391–403.

(104) Baerends, E. J.; Ziegler, T.; Atkins, A. J.; Autschbach, J.; Bashford, D.; Baseggio, O.; Bérces, A.; Bickelhaupt, F. M.; Bo, C.; Boerritger, P. M.; Cavallo, L.; Daul, C.; Chong, D. P.; Chulhai, D. V.; Deng, L.; Dickson, R. M.; Dieterich, J. M.; Ellis, D. E.; van Faassen, M.; Ghysels, A.; Giammona, A.; van Gisbergen, S. J. A.; Goez, A.; Götz, A. W.; Gusarov, S.; Harris, F. E.; van den Hoek, P.; Hu, Z.; Jacob, C. R.; Jacobsen, H.; Jensen, L.; Joubert, L.; Kaminski, J. W.; van Kessel, G.; König, C.; Kootstra, F.; Kovalenko, A.; Krykunov, M.; van Lenthe, E.; McCormack, D. A.; Michalak, A.; Mitoraj, M.; Morton, S. M.; Neugebauer, J.; Nicu, V. P.; Noodleman, L.; Osinga, V. P.; Patchkovskii, S.; Pavanello, M.; Peeples, C. A.; Philipsen, P. H. T.; Post, D.; Pye, C. C.; Ramanantoanina, H.; Ramos, P.; Ravenek, W.; Rodríguez, J. I.; Ros, P.; Rüger, R.; Schipper, P. R. T.; Schlüns, D.; van Schoot, H.; Schreckenbach, G.; Seldenthuis, J. S.; Seth, M.; Snijders, J. G.; Solà, M.; M, S.; Swart, M.; Swerhone, D.; te Velde, G.; Tognetti, V.; Vernooijs, P.; Versluis, L.; Visscher, L.; Visser, O.; Wang, F.; Wesolowski, T. A.; van Wezenbeek, E. M.; Wiesenekker, G.; Wolff, S. K.; Woo, T. K.; Yakovlev, A. L. ADF2018, SCM, Theoretical Chemistry, Vrije Universiteit, Amsterdam, The Netherlands, https://www.scm.com.

(105) Handy, N. C.; Cohen, A. J. Left-Right Correlation Energy. *Mol. Phys.* **2001**, *99* (5), 403–412.

(106) Baker, J.; Pulay, P. Assessment of the Handy–Cohen Optimized Exchange Density Functional for Organic Reactions. *J. Chem. Phys.* **2002**, *117* (4), 1441–1449.

(107) Van Lenthe, E.; Baerends, E. J. Optimized Slater-Type Basis Sets for the Elements 1–118. *J. Comput. Chem.* **2003**, *24* (9), 1142–1156.

(108) van Lenthe, E.; Baerends, E. J.; Snijders, J. G. Relativistic Total Energy Using Regular Approximations. *J. Chem. Phys.* **1994**, *101* (11), 9783–9792.

(109) Swart, M.; Ehlers, A. W.; Lammertsma, K. Performance of the OPBE Exchange-Correlation Functional. *Mol. Phys.* **2004**, *102* (23–24), 2467–2474.

(110) Xu, X.; Goddard, W. A. Assessment of Handy–Cohen Optimized Exchange Density Functional (OPTX). *J. Phys. Chem. A* **2004**, *108* (40), 8495–8504.

(111) Swart, M.; Solà, M.; Bickelhaupt, F. M. Density Functional Calculations of E2 and S_N2 Reactions: Effects of the Choice of Method, Algorithm, and Numerical Accuracy. *J. Chem. Theory Comput.* **2010**, *6* (10), 3145–3152.

(112) Gonzales, J. M.; Allen, W. D.; Schaefer, H. F. Model Identity S_N2 Reactions $CH_3X + X^-$ (X = F, Cl, CN, OH, SH, NH_2, PH_2): Marcus Theory Analyzed. *J. Phys. Chem. A* **2005**, *109* (46), 10613–10628.

(113) Franchini, M.; Philipsen, P. H. T.; van Lenthe, E.; Visscher, L. Accurate Coulomb Potentials for Periodic and Molecular Systems through Density Fitting. *J. Chem. Theory Comput.* **2014**, *10* (5), 1994–2004.

(114) Franchini, M.; Philipsen, P. H. T.; Visscher, L. The Becke Fuzzy Cells Integration Scheme in the Amsterdam Density Functional Program Suite. *J. Comput. Chem.* **2013**, *34* (21), 1819–1827.

(115) Fukui, K. The Path of Chemical Reactions - the IRC Approach. *Acc. Chem. Res.* **1981**, *14* (12), 363–368.

(116) Deng, L.; Ziegler, T.; Fan, L. A Combined Density Functional and Intrinsic Reaction Coordinate Study on the Ground State Energy Surface of H2CO. *J. Chem. Phys.* **1993**, *99* (5), 3823–3835.

(117) Deng, L.; Ziegler, T. The Determination of Intrinsic Reaction Coordinates by Density Functional Theory. *Int. J. Quantum Chem.* **1994**, *52* (4), 731–765.

(118) Sun, X.; Soini, T. M.; Poater, J.; Hamlin, T. A.; Bickelhaupt, F. M. PyFrag 2019—Automating the Exploration and Analysis of Reaction Mechanisms. *J. Comput. Chem.* **2019**, *40* (25), 2227–2233.

(119) Klamt, A.; Schüürmann, G. COSMO: A New Approach to Dielectric Screening in Solvents with Explicit Expressions for the Screening Energy and Its Gradient. *J. Chem. Soc. Perkin Trans. 2* **1993**, 799–805.

(120) Klamt, A. Conductor-like Screening Model for Real Solvents: A New Approach to the Quantitative Calculation of Solvation Phenomena. *J. Phys. Chem.* **1995**, *99* (7), 2224–2235.

(121) Klamt, A.; Jonas, V. Treatment of the Outlying Charge in Continuum Solvation Models. *J. Chem. Phys.* **1996**, *105* (22), 9972–9981.

(122) Pye, C. C.; Ziegler, T. An Implementation of the Conductor-like Screening Model of Solvation within the Amsterdam Density Functional Package. *Theor. Chem. Acc.* **1999**, *101* (6), 396–408.

(123) Martin, R. L.; Hay, P. J.; Pratt, L. R. Hydrolysis of Ferric Ion in Water and Conformational Equilibrium. *J. Phys. Chem. A* **1998**, *102* (20), 3565–3573.

(124) González-Fabra, J.; Castro-Gómez, F.; Sameera, W. M. C.; Nyman, G.; Kleij, A. W.; Bo, C. Entropic Corrections for the Evaluation of the Catalytic Activity in the Al(III) Catalysed Formation of Cyclic Carbonates from CO_2 and Epoxides. *Catal. Sci. Technol.* **2019**, *9* (19), 5433–5440.

(125) Ariai, J.; Gellrich, U. The Entropic Penalty for Associative Reactions and Their Physical Treatment during Routine Computations. *Phys. Chem. Chem. Phys.* **2023**, *25* (20), 14005–14015.

(126) Galabov, B.; Koleva, G.; Schaefer III, H. F.; Allen, W. D. Nucleophilic Influences and Origin of the S_N2 Allylic Effect. *Chem. – Eur. J.* **2018**, *24* (45), 11637–11648.

(127) Hansen, T.; Vermeeren, P.; Yoshisada, R.; Filippov, D. V.; van der Marel, G. A.; Codée, J. D. C.; Hamlin, T. A. How Lewis Acids Catalyze Ring-Openings of Cyclohexene Oxide. *J. Org. Chem.* **2021**, *86* (4), 3565–3573.

(128) Atkins, P.; Paula, J. de. *Atkins' Physical Chemistry*, 9th ed.; Oxford University Press: Oxford, 2010.

(129) Jensen, F. *Introduction to Computational Chemistry*, 3rd ed.; John Wiley & Sons, 2017.